Burrowing fauna mediate alternative stable states in the redox cycling of salt marsh sediments

van de Velde, Sebastiaan J.; Hidalgo-Martinez, Silvia; Callebaut, Ine; Antler, Gilad; James, Rebecca K.; Leermakers, Martine; Meysman, Filip J.R.

DOI
10.1016/j.gca.2020.02.021

Publication date
2020

Document Version
Accepted author manuscript

Published in
Geochimica et Cosmochimica Acta

Burrowing fauna mediate alternative stable states in the redox cycling of salt marsh sediments

Sebastiaan J. van de Velde [1,2#], Silvia Hidalgo-Martinez [3], Ine Callebaut [2], Gilad Antler [4,5], Rebecca K. James [6], Martine Leermakers [2], Filip J. R. Meysman [3,7]

[1] Department of Earth and Planetary Sciences, University of California, Riverside, CA 92521, USA
[2] Analytical, Environmental and Geo-Chemistry, Vrije Universiteit Brussel, 1050 Brussel, Belgium
[3] Department of Biology, Universiteit Antwerpen, 2610 Wilrijk, Belgium
[4] Department of Geological and Environmental Sciences, Ben-Gurion University of the Negev, Beersheba, Israel
[5] The Interuniversity Institute for Marine Sciences, Eilat, Israel
[6] Department of Estuarine and Delta Systems, NIOZ Royal Netherlands Institute for Sea Research and Utrecht University, 4401 NT Yerseke, The Netherlands
[7] Department of Biotechnology, Delft University of Technology, 2629 HZ Delft, The Netherlands
[#] Corresponding author: sebastiv@ucr.edu

Submitted to: Geochimica et Cosmochimica Acta
Keywords: bioturbation, marine sediments, redox cycling, salt marshes, alternative stable states
Version: revised version 4 (17/02/2020)
Word count: Abstract: 215 / Text: 8 547

ABSTRACT

The East Anglian salt marsh system (UK) has recently generated intriguing data with respect to sediment biogeochemistry. Neighbouring ponds in these salt marshes show two distinct regimes of redox cycling: the sediments are either iron-rich and bioturbated, or they are sulphide-rich and unbioturbated. No conclusive explanation has yet been given for this remarkable spatial co-occurrence. Here, we quantify the geochemical cycling in both pond types, using pore-water analyses and solid-phase speciation. Our results demonstrate that differences in solid-phase carbon and iron inputs are likely small between pond types, and so these cannot act as the direct driver of the observed redox dichotomy. Instead, our results suggest that the presence of bioturbation plays a key role in the transition from sulphur-dominated to iron-dominated sediments. The presence of burrowing fauna in marine sediments stimulates the mineralisation of organic matter, increases the iron cycling and limits the build-up of free sulphide. Overall, we propose that the observed dichotomy in pond geochemistry is due to alternative stable states, which result from non-linear interactions in the sedimentary iron and sulphur cycles that are amplified by bioturbation. This way, small differences in solid phase input can result in very different regimes of redox cycling due to positive feedbacks. This non-linearity in the iron and sulphur cycling could be an inherent feature of marine sediments, and hence, alternative stable states could be present in other systems.

1. INTRODUCTION

Most of the present day seafloor is inhabited by burrowing macrofauna (polychaetes, crustaceans, bivalves, etc.), that are considered ecosystem engineers, as they strongly alter the physical and chemical environment in which they live (Jones et al., 1994; Meysman et al. 2006). Benthic fauna affect the redox cycling of carbon, oxygen, iron, sulphur and other elements via feeding behaviour as well as burrow construction and movement (Aller, 1977; Aller and Aller, 1998; Meysman et al., 2006; Kristensen et al., 2012; van de Velde et al., 2018). They stimulate transport in the sediment by mixing of solid-phase particles (bio-mixing) and promote the exchange of pore-water solutes with the overlying water column (bio-irrigation). Bio-mixing and bio-irrigation are both lumped under the umbrella term 'bioturbation' (Kristensen et al., 2012) but have distinct effects on organic carbon mineralisation and early diagenesis (Kostka and Luther, 1994; Kostka et al., 2002; van de Velde and Meysman, 2016). Bio-irrigation stimulates aerobic respiration by introducing oxygen into deeper anoxic horizons (Archer and Devol, 1992), and it increases the efflux of reduced Fe^{2+} and H_2S from the sediment, thereby reducing recycling of Fe and S (Elrod et al., 2004; van de Velde and Meysman, 2016; Thibault de Chanvalon et al., 2017). Bio-mixing has an opposite effect; it transports organic matter past the oxic zone, thus decreasing aerobic respiration (Berner and Westrich, 1985), while at the same time, it increases the re-oxidation of iron sulphide minerals, and hence stimulates Fe and S recycling (Swider and Mackin, 1989; Canfield et al., 1993).

Recently, salt marshes along the North Sea coast of Norfolk (UK) have been found to host ponds that are either bioturbated or unbioturbated (Mills et al., 2016; Antler et al., 2019; Hutchings et al., 2019). Both pond types host oxygenated waters, but show distinct sediment geochemistries, which appears to belong to two redox end-members. In one type of pond, the sediments are heavily bioturbated and iron rich, while the sediments in a second type of pond do not have burrowing fauna and are sulphide rich. These two different redox states can be found in neighbouring ponds, less than five meters apart, which suggests that local boundary conditions are highly similar (Antler et al., 2019; Hutchings et al., 2019). These salt marsh pond sediments hence provide a unique environment to study the impact of bioturbation on sediment geochemistry, as they allow the effect of burrowing fauna to be quantified by comparing the geochemistry of the two oxygenated ponds.

The objective of this study is to better understand the differential geochemical cycling in the ponds of the East Anglian salt marsh system and to investigate the particular role of bioturbation. Recently, Antler et al. (2019) reported pore-water data, as well as carbon, sulphur and oxygen isotope data from the pond sediments, that clearly substantiate the redox dichotomy

and found that the redox state of a given pond remains stable over many years. Hutchings et al. (2019) presented a spatial survey of the East Anglian salt marsh system, and they proposed that the pond distribution could be partially controlled by differences in organic carbon or iron delivery. Here, we present new pore-water and solid-phase data from the East Anglian salt marsh ponds that were collected during three separate visits (in October 2015, August 2016 and August 2018). From these, we put forward a conceptual model that can explain the observed dichotomy in sediment biogeochemistry. The model suggests that the sediments exhibit alternative stable states and that bioturbation plays a crucial role in the formation of these alternative stable states.

2. MATERIALS & METHODS

2.1 Field site location

The Blakeney salt marsh (Fig. 1a-c; 52° 57' N, 01° 00' E) is part of a larger salt marsh complex that stretches for > 200 km along the North Sea coast of East Anglia (UK), and which was formed some hundreds years ago (Pethick, 1980; Funnell and Pearson, 1989). The higher marsh is vegetated, but contains several shallow, water-filled ponds, which have a surface area ~50 - 500 m^2 and a water depth of 10 – 20 cm (Fig. 1d,e). These ponds likely formed during the initial stage of marsh development from unvegetated patches (Pye et al., 1990) that were not stabilised by plant roots, and hence were more susceptible to erosion. Over time, these bare patches became depressions that subsequently evolved into ponds (Pethick, 1974).

The ponds in Blakeney salt marsh show a clear dichotomy in terms of their sediment geochemistry (Antler et al., 2019; Hutchings et al., 2019). Ponds are either bioturbated and iron-rich, or unbioturbated and sulphide-rich. Moreover, these two redox regimes are so divergent that they can be distinguished by visual inspection of the sediment surface (Antler et al., 2019; Hutchings et al., 2019). The sediment surface of the bioturbated ponds shows a bright reddish colour, most likely originating from high concentrations of iron oxides, and is intersected with *Nereis sp.* worm burrows (Figure 1e, estimated density ~1000 individuals m^{-2}; Antler et al., 2019). The sediments of the unbioturbated ponds are black (suggesting high concentrations of iron sulphides) and are often colonised by white mats of large sulphur oxidising bacteria (e.g. *Beggiatoa*) (Fig. 1e).

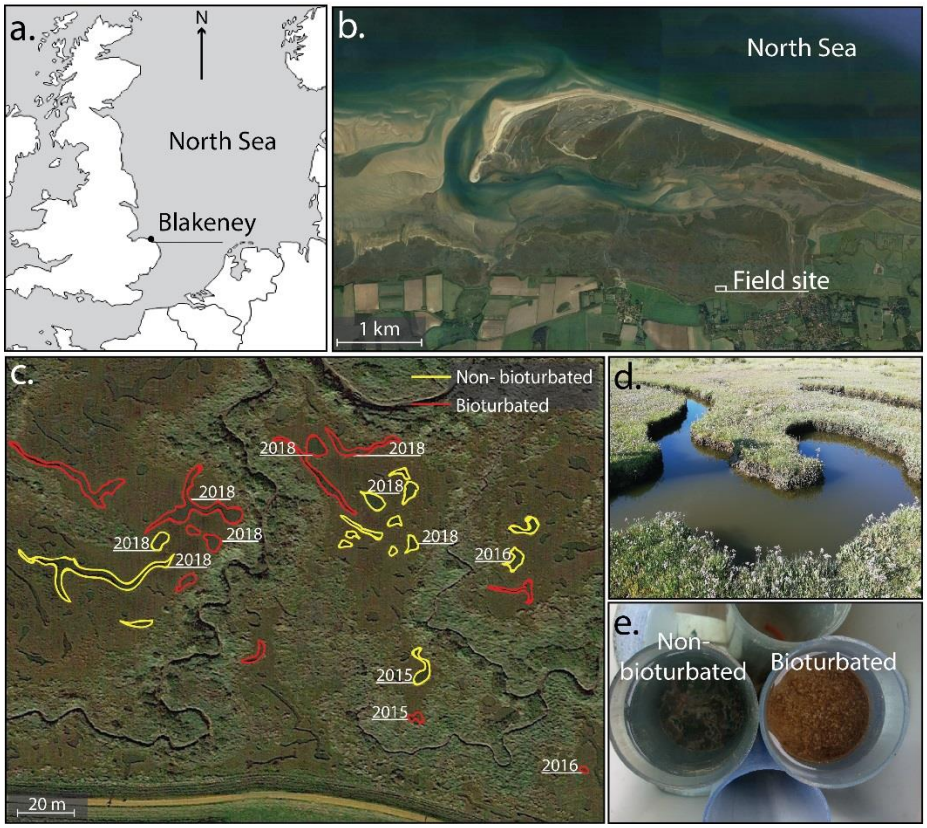

Figure 1: (a) Geographical location of the Blakeney Salt marsh along the Norfolk coast (UK). (b,c) Overview of the sampling locations. Aerial picture of the field site, with an indication of the unbioturbated (yellow outlining) and bioturbated (red outlining) ponds, based on visual inspection of sediment surface. The year annotation denotes the campaigns when the ponds were sampled (coordinates are given in Table 1). (d) Picture of a typical pond. (e) Pictures of the typical sediment surface of a bioturbated (reddish with worm burrows) and an unbioturbated (dark sediment covered with microbial mats) pond.

2.2 Sampling campaigns

Pond water samples and sediment cores were collected on three separate occasions (2015, 2016 and 2018). Twelve ponds were examined in total (sampling sites in Fig. 1c, coordinates in Table 1). During the first and second campaigns, one bioturbated pond and one unbioturbated pond were investigated. During the third campaign, four ponds from each type were sampled. In all three campaigns, the temperature (T), salinity (S) and oxygen (O_2) of the overlying water were recorded *in situ* using a portable MultiLine Multi 3430 IDS sensor (WTW, Germany). Additionally, pond water was collected for analysis of soluble reactive phosphorus (SRP), ammonium (NH_4^+), dissolved metals (dFe, dMn), dissolved inorganic carbon (DIC) and sulphate (SO_4^{2-}). In 2018, we conducted a small survey to map the spatial pond type distribution at the field site (Fig. 1c). Ponds were classified based on visual inspection at the sediment-water interface (sediment coloration and evidence of bioturbation; Fig. 1e) and the presence of dissolved sulphide in the pore water. The presence of sulphide was tested by inserting a silver wire in the sediment for 10 minutes. If the wire turned black, this indicated that Ag_2S had formed, and that the pore water contained high amounts of dissolved sulphide. If there was no

colour change, the pore water did not contain high levels of dissolved sulphide (Fig. A1, Appendix 4). The results of the silver wire assessment were always identical to the visual inspection of the sediment surface, suggesting that our pond classification procedure was consistent and robust.

Table 1: Coordinates and type of the ponds sampled in the 2015, 2016 and 2018 field campaigns in the Blakeney salt marsh with indication of analyses done on core samples (see main text for details). See Fig. 1c for relative geographical location of the ponds.

	Coordinates		Type	Year sampled	Core analyses	
					Pore water	*Solid Phase*
1	52° 57′ 22.7′′ N	01° 00′ 14.0′′ E	Bioturbated	2015	dFe, dMn, SO_4^{2-}, Cl^-, NH_4^+, ΣH_2S	porosity, grain size, POC, TN, ^{210}Pb, ^{137}Cs, Fe speciation, S speciation
2	52° 57′ 23.0′′ N	01° 00′ 14.0′′ E	Unbioturbated	2015	″	″
3	52° 57′ 22.2′′ N	01° 00′ 16.6′′ E	Bioturbated	2016	″	porosity, POC, TN, Fe speciation, S speciation
4	52° 57′ 24.0′′ N	01° 00′ 16.0′′ E	Unbioturbated	2016	″	″
5	52° 57′ 25.2′′ N	01° 00′ 13.2′′ E	Bioturbated	2018	-	porosity, grain size, POC, TN
6	52° 57′ 25.3′′ N	01° 00′ 12.5′′ E	Bioturbated	2018	-	″
7	52° 57′ 24.6′′ N	01° 00′ 10.6′′ E	Bioturbated	2018	-	″
8	52° 57′ 24.3′′ N	01° 00′ 10.9′′ E	Bioturbated	2018	-	″
9	52° 57′ 24.7′′ N	01° 00′ 13.4′′ E	Unbioturbated	2018	-	″
10	52° 57′ 24.4′′ N	01° 00′ 14.1′′ E	Unbioturbated	2018	-	″
11	52° 57′ 24.3′′ N	01° 00′ 9.9′′ E	Unbioturbated	2018	-	″
12	52° 57′ 24.1′′ N	01° 00′ 10.1′′ E	Unbioturbated	2018	-	″

During the 2015 campaign, 4 sediment cores were collected from each pond by manual insertion of transparent PVC core liners (6 cm inner diameter; 30 cm long). During retrieval and transport to the nearby field laboratory (~2 km away), care was taken to avoid disturbance of the sediment. To verify the integrity of our extraction procedure, pore water was collected in two alternative ways. In 2 replicate cores from each pond, pore water was extracted using rhizons within ~2h of sampling. Rhizons (pore size ~0.1 µm) were placed in predrilled holes along the length of the sediment core (replicate one: 1 cm intervals over 20 cm, replicate two: 2 cm intervals over 30 cm), and, subsequently, syringes were attached to the rhizons and manually withdrawn to create a vacuum and extract pore water (Fig. A2, Appendix 4). After 1 hour, syringes were detached, and the retrieved pore water was distributed into sampling vials without filtration (depending on the analyte, a fixative was added – see section 2.4). The remaining 2 replicate cores were left overnight in an incubation tank filled with water collected from the sampling site. The incubation tank was located in a climate-controlled room at *in-situ* temperature and bubbled with air to retain 100% air saturated oxygen levels. The next day, the two cores were sectioned for pore-water extraction in an anaerobic glove box (N_2 atmosphere; Coy lab products, USA). Slicing was carried out at 0.5 cm intervals from 0 to 3 cm depth, at 1

cm intervals between 3 and 8 cm depth, and in 2 cm slices from 8 to 22 cm depth. Sediment sections were collected in 50 mL centrifuge tubes (polypropylene; TPP, Switzerland) and centrifuged at 2500g for 10 min (Sigma 3-18KS, Sigma Laborzentrifugen GmbH, Germany). Subsequently, the centrifuge tubes were opened in the glove box, pore water was filtered through 0.42 µm cellulose acetate filters (Chromafil Xtra) and distributed into sampling vials (depending on the analyte, a fixative was added – see section 2.4). The solid phase that remained after centrifugation was freeze-dried and stored in an aluminium bag under nitrogen atmosphere for solid-phase analyses and radionuclide measurements.

During the 2016 campaign, pore-water retrieval was largely similar to the first campaign, with the difference that core sectioning took place immediately after core collection. Pore water was retrieved by rhizons in 2 replicates cores, while the other two cores were sliced in a portable glove bag filled with N_2-gas (Captair Field Pyramid, Erlab, France) within 2 h after core collection. The oxygen level in the glove bag was continuously monitored (Teledyne 3110 equipped with a trace oxygen sensor). Core sectioning and processing was as in the first campaign.

Pore-water samples from the first two campaigns were analysed for metals (dFe, dMn), anions (SO_4^{2-}, Cl^-), ammonium (NH_4^+) and total free sulphide ($\Sigma H_2S = [H_2S] + [HS^-]$). Cations and anions were always analysed from the pore water extracted via core slicing. To avoid loss of gaseous H_2S upon exposure of pore water to the atmosphere, ΣH_2S was always analysed from the pore water obtained through rhizons and stabilised with ZnAc (see section 2.4). In 2015, NH_4^+ was analysed on the rhizon samples, while in 2016 it was analysed on the centrifugated pore water.

During the 2018 campaign, two cores for solid-phase analyses were collected from each investigated pond. Cores were immediately sliced in open air in the field, and no pore water was collected. Sediment samples were transferred to 50 ml centrifuge tubes (polypropylene; TPP, Switzerland) and transported to the University of Antwerp (transit time ~12 hours), freeze dried and analysed for carbon and nitrogen content as well as sediment grain size distribution. Additionally, plant material from the 7 most common plants on the high marsh (*Suaeda maritima*, *Salicornia radicans*, *Spartina anglica*, *Armenia maritima*, *Elytrigia atherica*, *Halimione portulacoides* and *Limonium vulgare*) was collected, oven dried at 70°C and analysed for total carbon, nitrogen and phosphorus content.

2.3 Sediment parameters

Sediment grain size and sorting was determined on sediment slices from four depth horizons (1-1.5 cm, 5-6 cm, 12-14 cm and 20-22 cm) on one core from each pond sampled in 2015 and 2018 (5 replicate analyses per pond type). Grain size distribution was determined by laser diffraction (Malvern Mastersizer 2000) after homogenisation and rewetting of freeze-dried sediment (McCave, 1986). Solid-phase density from each depth slice of all cores sampled in 2015 and 2016 was determined by adding a known mass of ground, freeze-dried sediment to a 100 ml graduated cylinder filled with tap water and recording the volume displacement. Sediment porosity (volume of pore water per total volume of sediment) from each depth slice of all cores sampled in all three of the campaigns (2 replicate depth profiles per pond type; Table 1) was determined from water content and solid-phase density measurements, considering the salt content of the pore water. The water content of the sediment was determined as the difference in weight before and after freeze-drying.

2.4 Bottom-water and pore-water analyses

In 2015, samples for DIC analysis were collected in 5 mL headspace vials, left to overflow and fixed with 10 µL of a saturated $HgCl_2$ solution. Analysis was done using an AS-C3 analyzer (Apollo SciTech, USA), consisting of an acidification and purging unit in combination with a LICOR-7000 CO_2/H_2O Gas Analyzer (precision 0.3%). Quality assurance was done by regular analysis of Certified Reference Materials (CRM) obtained from the Scripps Institution of Oceanography (Batch 140; Dickson et al., 2003). In 2018, sample collection was identical, but the sampling vials were 12 mL gastight Exetainer vials (Labco). Analysis was done on an elemental analyser (EuroVector Euro EA 3000, precision < 10 %). Prior to analysis, exetainer vials were injected with He to create a 4 mL headspace, acidified with phosphoric acid (100 µL, 99 %, Sigma-Aldrich) and then equilibrated on a rotatory shaker for 12 h.

Samples (250 µl) for dissolved metal analysis (dFe, dMn) were stabilised with 50 µL/mL bidistilled HNO_3 (65%, suprapure, Merck) and stored at 4°C. Samples collected in 2015 were diluted 50x with a standard matrix solution containing 35 salinity artificial seawater, 2% HNO_3 and 0.2 mg L^{-1} Ytterbium as an internal standard (Crompton, 1989). Analysis was done by Inductively Coupled Plasma – Optical Emission Spectroscopy (ICP-OES, ThermoFisher iCAP6500; precision < 2%, Limit of Quantification - LOQ = 0.02 µM for dFe and dMn), which was calibrated using external standard solutions and quality controlled by regular analysis of ICP multi-element IV CRM. Samples collected in 2016 and 2018 were diluted 20x with a 1% HNO_3 solution and analysis was done by High Resolution - Inductively Coupled Plasma – Mass

Spectroscopy (HR-ICP-MS, ThermoScientific Element 2, precision < 5%, LOQ = 5 nM for dFe and 1 nM for dMn), which was calibrated using external standard solutions and quality controlled by regular analysis of SLRS-6 and 1640 CRM. Indium (2.5 ppb) containing 2% HNO_3 was injected simultaneously as an internal standard. Note that we employ the operational term 'dissolved' iron and manganese (dFe, dMn), as we measured the total concentration of iron and manganese after passage through a 0.42 µm filter, which can contain colloidal or nanoparticulate iron and manganese (with different oxidation states) (Raiswell and Canfield, 2012).

Samples (250 µL) for SO_4^{2-} and Cl^- analyses were fixed with 100µL ZnAc (5%) per mL, to avoid oxidation of free sulphide to sulphate. After 10x dilution, samples were analysed by ion chromatography, using an isocratic eluent (3.5 mM Na_2CO_3 / 1 mM $NaHCO_3$) combined with a Dionex AS-14 analytical column (Thermo Scientific) and conductivity detection (ED40 electrochemical detector) with a precision of 8% and a LOQ of 0.005 mM for both Cl^- and SO_4^{2-} (Gros et al., 2008). The instrument was calibrated using external standards and quality controlled by regular analysis of a control sample (Quasimeme, QNU 253 ew). Reported SO_4^{2-} concentrations were normalised for chloride content ($[SO_4^{2-}]_{corrected} = [SO_4^{2-}]_{measured} / [Cl^-]_{measured} * \overline{[Cl^-]}_{measured}$), to account for salinity gradients that occur in these salt marsh sediments (Mills et al., 2016).

Nutrient samples (NH_4^+, SRP) were diluted 25 times with a low nutrient seawater matrix solution and analysed by a SEAL QuAAtro segmented flow analyser (precision < 4%, LOQ = 0.2µM for NH_4^+ and 0.1 µM for SRP), which was calibrated using external standards and quality controlled by regular interlaboratory comparisons (Aminot et al., 2009).

Subsamples (1 ml) for free sulphide analysis were fixed with 100 µL of ZnAc (5%) per mL of sample, and measured spectrophotometrically using the method of Cline (Cline, 1969) (precision not determined).

2.5 Radionuclides

Subsamples of one replicate core from each pond studied in 2015 were analysed for ^{210}Pb and ^{137}Cs activity at Utrecht University. Samples for ^{210}Pb were spiked with ^{209}Po and subsequently microwave digested in 10 mL HCl (concentrated) for 3h. Afterwards, 2 mL 3.5% $HClO_4$ was added and the mixture was evaporated to remove the acids. The precipitate was then re-dissolved in 5 mL HCl (concentrated) for 30 min. Subsequently, 40 mL of boric acid (12 g L^{-1} in 0.5M HCl), 4 mL NH_4OH and 5 mL of ascorbic acid (40 g L^{-1} in 0.5M HCl) were added and Po isotopes were deposited by suspending a silver disk in the solution, which was

heated to 80°C for 4h and left overnight. Counting of ^{210}Po was done using a Canberra Passivated Implanted Planar Silicon detector (Canberra Industries, USA), allowing the ^{210}Pb activity to be calculated (precision < 5%). $^{210}Pb_{excess}$ was calculated by subtracting the average of ^{214}Pb and ^{214}Bi activity (which represents the ^{210}Pb activity in equilibrium with ^{226}Ra) from the total ^{210}Pb value.

The sedimentation flux is the amount of solids that pass through a given sediment horizon (when a coordinate system is tied to the sediment-water interface). If we assume that sediment compaction is in steady state (any changes with depth in porosity are balanced by changes in sedimentation velocity), the sedimentation flux J_s (expressed in kg m^{-2} yr^{-1}) is constant throughout the whole sediment column (Meysman et al., 2005). The mean sedimentation velocity over a given sediment layer can be calculated as

$$v = J_s / \left(\left(1 - \phi_{AVG} \right) \rho_s \right) \quad [1]$$

where ϕ_{AVG} is the mean porosity in the sediment layer. The Periodic Flux model (PF; Sanchez-Cabeza et al., 2000) was fitted to the $^{210}Pb_{excess}$ profile of the unbioturbated core to determine the sedimentation flux and sedimentation velocity. The PF model is a generalisation of the more widely used constant flux model (Appleby and Oldfield, 1978), and is valid when the flux of $^{210}Pb_{excess}$ to the sediment is variable. To validate the PF model, we used an independent tracer (^{137}Cs; Sanchez-Cabeza and Ruiz-Fernández, 2012). The sedimentation flux can be calculated from the ^{137}Cs depth profile according to

$$J_s = \frac{\rho_S}{\tau} \int_0^L \left(1 - \phi(x) \right) dx \quad [2]$$

Where L is the depth of the ^{137}Cs peak and τ is the known time since ^{137}Cs peak input (which was assumed to be the year 1963).

The bioturbated core experienced sediment mixing, and hence the PF model could not be applied to the corresponding $^{210}Pb_{excess}$ profile. Alternatively, we used the peak depth of the ^{137}Cs depth profile to determine the sedimentation flux (eq. [2]). Furthermore, because our data indicated a highly variable ^{210}Pb flux, the scatter on the data did not allow to constrain a mixing depth or bio-diffusion coefficient from the $^{210}Pb_{excess}$ profiles (Lecroart et al., 2010).

2.6 Solid-phase analyses

Freeze-dried samples and oven-dried plant samples were ground to a fine powder and analysed by an Interscience Flash 2000 organic element analyser (precision <5%) for determination of particulate organic carbon (POC) and total nitrogen (TN). Before analysis and

after weighing, samples for POC were first acidified with 0.1M HCl to remove the inorganic carbon (Nieuwenhuize et al., 1994). Concentrations of POC are expressed as mass % of dry sediment. The C:N ratio of the organic matter in the sediment was calculated as the ratio of POC over TN (C_{org}:N_{tot}).

Freeze-dried sediment subsamples (300 mg) from each sediment horizon sampled in 2015 and 2016 were used for sequential iron extraction as described by Poulton and Canfield (2005). This extraction determines 4 operational iron phases: (i) carbonate associated iron + acid-volatile sulphide ($Fe_{carb+AVS}$), (ii) easily reducible iron oxides (Fe_{ox1}), (iii) moderately reducible iron oxides (Fe_{ox2}) and (iv) magnetite (Fe_{mag}). Iron associated with sulphide (Fe_{AVS}) and pyrite-iron (Fe_{pyr}) were determined in a separate extraction procedure (as discussed below). The extraction solutions and extraction times are summarised in Table A1 (Appendix 3). At the beginning of each extraction step, 10 mL of extraction solution was added, and the sample was extracted under constant agitation. Subsequently, the sample was centrifuged (2500g for 10 min) and the supernatant was filtered (0.45 µm cellulose acetate) and stored at 4°C for later analysis on ICP-OES (similar procedure as for pore-water samples). The next extraction step was started immediately, and all steps were executed inside a nitrogen-filled glove box.

Sediment subsamples (300 mg) from each sediment horizon sampled in 2015 and 2016 were analysed for acid-volatile sulphide (AVS) and chromium reducible sulphide (CRS) with a cold, two-step distillation procedure (Kallmeyer et al., 2004), based on the methods of Canfield et al. (1986) and Cornwell and Morse (1987). Freeze-dried sediment was directly weighed in the distillation flasks, which was immediately purged with N_2-gas. The first step extracts the AVS fraction via addition of a 6M HCl solution. H_2S is stripped from solution using N_2 as a carrier gas, and subsequently trapped in a 10 mL zinc acetate solution (5 %), with a drop of antifoam. After 40 min., the trap is replaced and 20 mL of N,N di-methyl formamide (DMF) is added to the distillation flask to solubilise the elemental sulphur fraction, followed by 12 mL of a reduced chromium solution (Table A1, Appendix 3). The H_2S released is trapped in an identical way as for the AVS fraction. The sulphide in the ZnAc traps is measured spectrophotometrically using the method of Cline (1969). For subsequent calculations, we assume that AVS consists primarily of iron monosulphide minerals (FeS) (Cornwell and Morse, 1987), and the CRS fraction contains both elemental sulphur (S^0) and pyrite (FeS_2) (Kallmeyer et al., 2004). To determine the elemental sulphur content, 10 mL of methanol was added to a separate subsample (300 mg) and the mixture was left to agitate overnight. Afterwards, the sample was centrifuged and cyclo-octasulphur was measured by ultrahigh pressure liquid chromatography (UPLC) using a Waters Acquity H-class instrument with a Waters column (methanol eluent 0.4 ml min-

[1] , Acquity UPLC BEH C18, 1.7-µm, 2.1 x 50 mm column; Waters, Japan) and detected by absorbance at 265 nm on a Waters PDA detector (Kamyshny et al., 2009), using external standards (reproducibility ~6%). CRS concentrations were corrected for S^0 content (S_{pyr} = CRS – S^0). Similarly, $Fe_{carb+AVS}$ in the iron speciation was corrected for Fe_{AVS} ($Fe_{carb} = Fe_{carb+AVS} - Fe_{AVS}$, assuming all AVS was FeS). Results of the sulphur speciation are reported in µmol g^{-1} of dry sediment and total inorganic sulphur is calculated as S_{inorg} = AVS + S^0 + S_{pyr}. Pyritic iron (Fe_{pyr}) is calculated assuming a stoichiometric ratio of 1:2 Fe:S for the S_{pyr} fraction. For clarity, iron speciation is reported in % of the total reactive iron fraction (Fe_{reac} = Fe_{carb} + Fe_{AVS} + Fe_{ox1} + Fe_{ox2} + Fe_{mag} + Fe_{pyr}).

2.7 Diffusive fluxes, burial rates and cycling numbers

Diffusive fluxes of dissolved species were calculated based on the pore-water profiles, using Fick's first law:

$$J_{diff} = -\phi \frac{D_0(S,T)}{\theta^2} \frac{\partial C}{\partial x} \quad [3]$$

where J_{diff} is the diffusive flux, C is the concentration in the pore water, x is the depth into the sediment, ϕ represents porosity, and θ^2 is the correction factor for sediment tortuosity ($\theta^2 = 1 - 2\ln\phi$) (Boudreau, 1996). The molecular diffusion coefficient (D_0) is calculated based on salinity and temperature using the R package CRAN:marelac (Soetaert et al., 2010), which is based on the constitutive relations presented in Boudreau (1997). The concentration gradient, $\partial C/\partial x$, was calculated by the linear regression from the concentration profiles at specific depths in the sediment. Sulphide fluxes where calculated from the total free sulphide concentration gradient but using the diffusion coefficient of HS^-. Sulphate fluxes were derived from uncorrected sulphate profiles (thus before rescaling for the Cl^- concentration).

Burial fluxes of POC, TN, all inorganic sulphide fractions and all reactive iron fractions were calculated based on the sedimentation flux (J_s) as derived from the radionuclide profiles and the concentration of the solid component at the bottom of the sediment column (C_{solid}):

$$J_{burial} = J_s C_{solid} \quad [4]$$

The cycling number, which represents the number of times an element is reduced before being buried, can be calculated as the ratio of the total reduction rate R_{red}^{tot} over the total burial

flux J_{burial} (Canfield et al., 1993)

$$N = \frac{R_{red}^{tot}}{J_{burial}} \quad [5]$$

2.8 Statistics

Where reported, the uncertainty (SE) associated with a calculated value x (not derived from direct measurements) are calculated based on the standard propagation of errors. For the statistical analyses, each pond was considered an independent replicate, and duplicate measurements were averaged to get a single value for each pond. Comparisons of POC concentrations and C_{org}:N_{tot} ratios of organic matter were not expected to vary over time, and therefore, measurements from all three sampling campaigns were used in a one-way ANOVA to compare between the bioturbated and unbioturbated pond types (n = 6). Comparisons of the nutrient, anion, cation and DIC concentrations for the replicate ponds were also conducted with a one-way ANOVA, using only the measurements from 2018 to avoid seasonal differences (n = 4). Residuals were tested for normality and homoscedasticity, and passed these assumptions, and p-values less than 0.05 were considered significant.

3. RESULTS

3.1 Bottom water conditions

The salinity was similar in the two pond types in each campaign but varied substantially between campaigns (range 24-44; Table 2). This indicates that the ponds experience a similar hydrological regime, consisting of regular flushing with North Sea seawater (S~34), combined with the seasonal dynamics of meteoric input and evaporation. In 2015, the water was clear in both pond types, which contrasted with 2016 and 2018, when the water of the unbioturbated ponds was colonised by green macroalgae (Fig. A3, Appendix 4). The sediment surface of the bioturbated ponds showed faecal casts, thus providing visual evidence for the presence of *Arenicola* spp.. During sediment core processing, we found *Nereis* sp. in the bioturbated cores (Fig. A4, Appendix 4), consistent with previous observations (Antler et al., 2019; Hutchings et al., 2019). In 2015, the daytime oxygen level was considerably lower in the unbioturbated (25% air saturation) than in the bioturbated pond (79%). In 2016 and 2018, oxygen was supersaturated in all ponds (Table 2), coincident with the presence of photosynthesizing macroalgae in the unbioturbated ponds. After filtration of bioturbated pond water, filters were distinctly green in colour, likely due to the presence of pelagic microalgae or resuspended microphytobenthos. Nutrient and metal concentrations in the ponds varied between sampling times, but a

comparison of replicates from 2018, showed no clear pattern with pond type (Table 2). Sulphate concentrations mainly varied with salinity. DIC concentrations were higher in the bioturbated ponds, but this was not statistically significant (One-way ANOVA, F-value$_{1,6}$ = 5.167, p = 0.06).

Table 2: Summary of bottom-water conditions, sediment and salt marsh plant properties for the two different pond types per sampling time. Errors represent the standard deviation of all measured samples (mean ± 1 s.d; $n_{(2015\ \&\ 2016)}$ = 3, $n_{(2018)}$ = 12). Three measurements were made per pond, Values without standard deviation are from single measurements. *Salinity for the 2015 campaign was derived from the Cl^- content in the overlying water.

Parameter	Symbol	Units	Unbioturbated pond			Bioturbated pond		
			2015	2016	2018	2015	2016	2018
# ponds measured			1	1	4	1	1	4
Bottom water conditions								
Temperature	T	°C	10.0	17.0	26 ± 2	10.3	19.1	26 ± 2
Salinity	S	-	31*	27	44 ± 4	30*	26	43 ± 2
pH	-	-	7.61 ± 0.03	7.8 ± 0.2	8.3 ± 0.1	7.9 ± 0.3	7.6 ± 0.1	8.0 ± 0.1
Oxygen concentration	-	% air saturation	25	>100	>100	79	>100	>100
DIC concentration	-	mM	3.91 ± 0.01	NA	4.2 ± 0.7	4.69 ± 0.01	NA	5.2 ± 0.5
NH_4^+ concentration	-	µM	8.1 ± 0.5	5.4 ± 0.4	6 ± 2	8.0 ± 0.6	0.6 ± 0.2	5 ± 2
SRP concentration	-	µM	0.3 ± 0.1	0.4 ± 0.1	2 ± 1	1.7 ± 0.1	11.3 ± 0.4	4 ± 4
SO_4^{2-} concentration	-	mM	24.3 ± 0.1	21.9 ± 0.2	33 ± 8	22.0 ± 0.3	19.3 ± 0.1	32 ± 9
dFe concentration	-	µM	<LOD	0.16 ± 0.01	0.9 ± 0.7	<LOD	0.5 ± 0.1	0.8 ± 0.6
dMn concentration	-	µM	<LOD	5.96 ± 0.03	5 ± 2	2.4 ± 0.1	5.7 ± 0.1	3 ± 1
Sediment properties (depth-averaged)								
C:N ratio	C_{org}:N_{tot}	-	12 ± 1	12 ± 2	13 ± 1	11 ± 1	11.9 ± 0.7	12.8 ± 0.9
Porosity	ϕ	-	0.88 ± 0.06	0.86 ± 0.07	0.86 ± 0.04	0.79 ± 0.09	0.83 ± 0.07	0.81 ± 0.06
Solid-phase density	ρ_{solid}	g cm^{-3}	2.2 ± 0.2	1.6 ± 0.3	-	2.1 ± 0.2	2.0 ± 0.5	-
Sedimentation	v_0	cm yr^{-1}	0.3 ± 0.1	-	-	0.3 ± 0.1	-	-
sedimentation flux	J_{sed}	g cm^{-2} yr^{-1}	0.08 ± 0.02	0.07 ± 0.03	-	0.13 ± 0.05	0.10 ± 0.04	-
Salt marsh plant properties								
		Suaeda maritima	*Salicornia radicans*	*Spartina anglica*	*Armenia maritima*	*Elytrigia atherica*	*Halimione portulacoides*	*Limonium vulgare*
C:N ratio	C_{org}:N_{tot}	18	20	27	20	74	26	25
C:P ratio	C_{org}:P_{tot}	682	492	669	554	1289	802	692

3.2 Porosity, radionuclides (^{210}Pb, ^{137}Cs) and sediment accumulation rate

All porosity profiles started from a similar high value (~0.95) and decreased with depth (Fig. 2a,b), consistent with the effect of compaction on marine sediments (Boudreau et al., 1998). The porosity-depth profile did not differ between sampling campaigns, but porosity profiles in the bioturbated cores showed more variability than in unbioturbated cores (Fig. 2a,b), consistent with an increase in textural heterogeneity due to burrowing fauna. Solid-phase density did not show any trend with depth (data not shown), nor was there any difference between pond types (Table 2). The unbioturbated ponds had a solid-phase density of 1.9 ± 0.4 g cm^{-3}, a median grain size of 13-21 µm and >74% of the particles were finer than 63 µm. The bioturbated ponds

had a solid-phase density of 2.0 ± 0.5 g cm^{-3}, a median grain size of 11-16 µm and >85% of the particles were finer than 63 µm. These solid-phase densities are lower than those of common siliclastic sediments (~2.6 g cm^{-3}), which is likely due to the high organic matter content (> 5% OC, see below) of the sediment.

The down-core variation in the $^{210}Pb_{excess}$ profiles is indicative for a variable depositional environment (Fig. 2c,d). When applied to the $^{210}Pb_{excess}$ data from the unbioturbated pond, the PF model (section 2.6) estimated a sedimentation flux of J_s = 0.8 ± 0.2 kg m^{-2} yr^{-1} and a sedimentation velocity ν_{sed} = 0.3 ± 0.1 cm yr^{-1}, which lies centrally within the wide range of values previously estimated for the Blakeney salt marsh (0.05 – 0.7 cm yr^{-1}; French, 1993). The narrowly defined peak in the ^{137}Cs activity profile from the unbioturbated pond suggests that the sediment has experienced very little mixing over the last decades. This contrasts with the smoothened ^{137}Cs peak in the depth profile from the bioturbated pond, which is typical for well-mixed sediments (Robbins et al., 1979) (Fig. 2e,f). The ^{137}Cs maxima can be found at 15 cm depth in the unbioturbated pond, and at 11 cm depth in the bioturbated pond (Fig. 2e,f). If we calculate a sedimentation flux according to eq. [2], we get at a ^{137}Cs-based sedimentation flux J_s = 0.91 ± 0.08 kg m^{-2} yr^{-1} for the unbioturbated pond and J_s = 0.86 ± 0.08 kg m^{-2} yr^{-1} for the bioturbated pond. Both values are indistinguishable from the sedimentation flux estimated based on the ^{210}Pb profile in the unbioturbated pond (0.8 ± 0.2 kg m^{-2} yr^{-1}; Table A2, Appendix 3). In the rest of this manuscript, we will use an average of all three estimates; J_s = 0.9 kg m^{-2} yr^{-1} and ν_{sed} = 0.3 cm yr^{-1}. This sedimentation flux is at the low end of the typical range for shallow environments (range: 0.3 – 10 kg m^{-2} yr^{-1}; Aller, 2014).

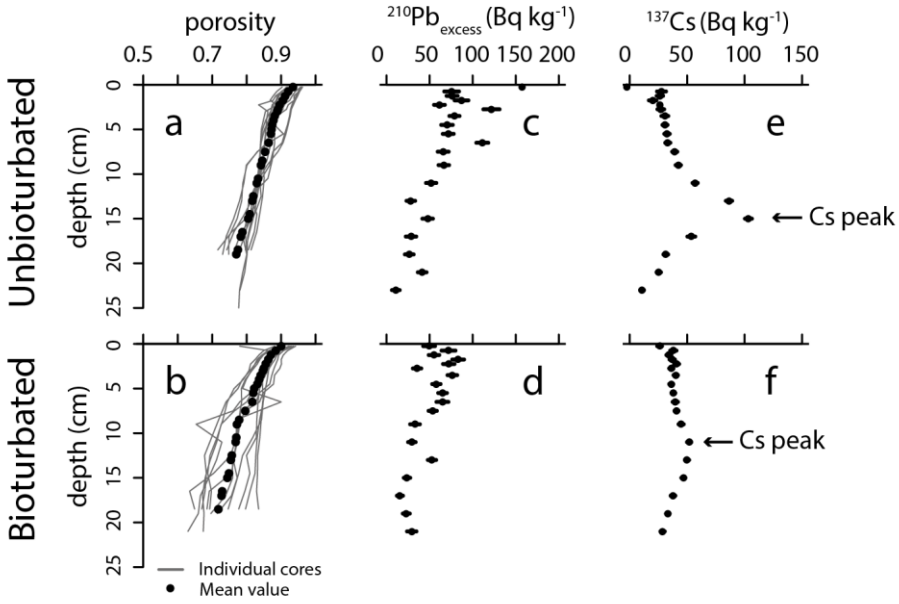

Figure 2: (a,b) Porosity depth profiles collected during 2015, 2016 and 2018 campaigns. (c,d) Excess ^{210}Pb depth profiles and (e,f) ^{137}Cs depth profiles collected in 2015. The Cs peak is indicated by the arrow and corresponds to the year 1963. Data are given for unbioturbated (top row) and bioturbated (bottom row) ponds

3.3 Solid-phase chemistry

Particulate organic carbon (POC) contents and C_{org}:N_{tot} ratios were measured on duplicate cores from each pond type in 2015 and 2016, as well as in duplicate cores from 4 different ponds of each pond type in 2018. POC depth profiles showed considerable variation, suggesting spatial heterogeneity in local input, possibly due to differences in macroalgal coverage (Fig. 3a,b). Overall, the depth-averaged POC was significantly higher in the unbioturbated ponds (7 ± 2 %) than in the bioturbated ponds (5.1 ± 0.9 %) (One-way ANOVA, F-value$_{1,10}$ = 15.53, p = 0.003) (Fig. 3c).

The depth averaged C_{org}:N_{tot} ratios (11-13; Table 2, Fig. 3d,e,f) were not significantly different between pond types (One-way ANOVA, F-value$_{1,10}$ = 0.195, p = 0.67), and are substantially lower than the C:N ratio of the common salt marsh vegetation (18-74) at the field site (Table 2). This suggests that ponds had the same source of organic matter, likely derived from a combination of marine (macroalgae, microphytobenthos) and terrestrial (surrounding marsh plants) origin. All cores showed an increase of the C_{org}:N_{tot} ratio with depth, suggesting preferential nitrogen mineralisation. The gradient in the C_{org}:N_{tot} ratio was less pronounced for the bioturbated cores, as expected from sediment bio-mixing (Fig. 3d,e).

Reactive iron was measured on duplicate cores from each pond type in 2015 and 2016. Total reactive iron (Fe_{reac} = Fe_{AVS} + Fe_{carb} + Fe_{ox1} + Fe_{ox2} + Fe_{mag} + Fe_{pyr}) showed substantial variation between depth profiles (Fig. 3g,h), but all cores had a similar depth-averaged iron content (280-

300 µmol g^{-1}) (Fig. 3i) (no statistics were done because of the small number of replicates; n = 2 for each treatment).

Total solid-phase contents of Al, Ti, Fe and Mn were determined on sediment cores collected in 2015 and 2016. Depth profiles of Ti/Al, Fe/Al and Mn/Al are indistinguishable between ponds, indicating that sites receive similar detrital inputs (Fig. 3j-r). All profiles deviate from the ratio of the average upper crust, which is not unexpected since they represent an isolated system, which can receive detrital matter of a given signature that does not need to represent the averaged signal of the upper crust.

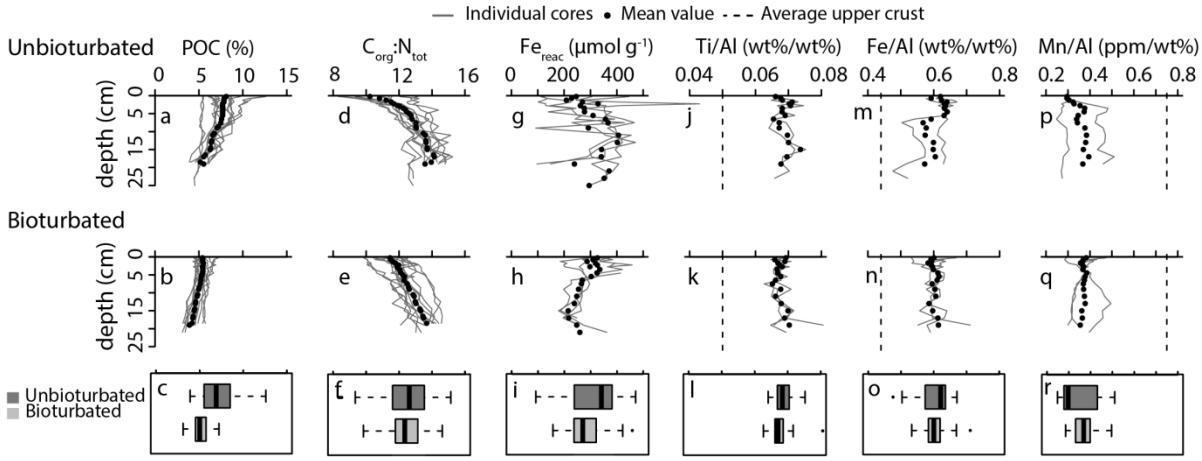

Figure 3: Vertical depth profiles of (a)-(b) particulate organic carbon (POC) collected in 2015, 2016 and 2018, (d)-(e) C:N ratio of organic matter (C_{org}:N_{tot}) collected in 2015, 2016 and 2018, (g)-(h) total solid-phase reactive iron (Fe_{reac}) collected in 2015 and 2016, (j)-(q) solid-phase element ratios collected in 2015 and 2016 recorded in the unbioturbated (top row) and bioturbated ponds (bottom row). (c)-(i) boxplots of the concentrations per pond type. Concentrations are expressed in µmol g^{-1} of dry sediment for Fe_{reac} or in mass % (gram per gram of dry sediment) for POC, ratios are in wt%/wt% (C_{org}:N_{tot}, Ti/Al and Fe/Al) or ppm/wt% (Mn/Ti). The dashed line is the ratio of the average upper crust, following McLennan (2001); Ti/Al = 0.05 wt%/wt%, Fe/Al = 0.44 wt%/wt%, Mn/Al = 0.75 ppm/wt%.

3.4 Iron and sulphur speciation

Solid-phase iron and sulphur speciation was determined on duplicate cores for each pond type in 2015 and 2016. Duplicate cores showed good agreement (Fig. 4). The depth profiles of iron speciation showed strong similarity between seasons but marked differences between pond types. In the unbioturbated cores, the oxidised fractions (Fe_{ox1}, Fe_{ox2}, Fe_{mag}) contributed ~30 % to the total pool of reactive iron (Fe_{reac}) in the upper 5 cm, after which their importance decreased to <10% in the deeper layers. Iron mono-sulphides (Fe_{AVS}) were the major component in the upper 5 cm (~50 %), below 5 cm pyrite (Fe_{pyr}) became the dominant fraction (> 80 % at 20 cm depth; Fig. 4a,b,e,f). In contrast, in the bioturbated pond, the oxidised fractions (Fe_{ox1}, Fe_{ox2}, Fe_{mag}) were dominant throughout the cores (50 – 100 %; Fig. 4c,d,g,h), while Fe_{AVS} build-up was restricted to the upper layers in 2015 (~50 % at 5 cm), after which it decreased to 0 % below 10 cm. In 2016, the oxidised fractions (Fe_{ox1}, Fe_{ox2}, Fe_{mag}) were also dominant, and the AVS build-up was limited and restricted to the deeper layers (~20 - 30 % of

439 the Fe_{reac} pool). In the deepest sediment layer analysed (at 19 cm depth), pyrite suddenly became
440 important (~50 % of the Fe_{reac} pool; Fig. 4d,h). This feature was present in both duplicate cores,
441 suggesting this is not an artefact.
442 Inorganic sulphur (S_{inorg}) rapidly accumulated with depth in the unbioturbated cores. In the
443 first 5 cm, AVS was the most important fraction (~200 µmol g^{-1}) in the total S_{inorg} pool, while
444 S^0 was only a small constituent. Below ~10 cm depth, pyrite became the major component (>
445 90 %) of the total S_{inorg} pool (Fig. 4i,m). In 2016, S^0 remained a minor constituent, while AVS
446 did not show an accumulation, and stayed constant (50 - 100 µmol g^{-1}) throughout the core (Fig.
447 4j,n). In the bioturbated cores of 2015, AVS showed an accumulation in the upper 10 cm (up
448 to 200 µmol g^{-1}), that disappeared with depth without being converted to S_{CRS} (Fig. 4k,o). In
449 2016, AVS accumulated slowly to ~150 µmol g^{-1} at 10 cm depth, and subsequently decreased
450 with depth (Fig. 4l,p). The small amounts of pyrite found throughout the cores were likely an
451 artefact from the extraction procedures (pyrite is determined as the difference between the CRS
452 fraction and the S^0 extraction). Nevertheless, the increased pyrite concentration in the last
453 sediment section of 2016 was found in both replicates, which indicates that this is likely not an
454 artefact. Pyrite appeared below 20 cm depth, which correlates with the expected burrowing
455 depth of local burrowing species *Nereis diversocolor* (15-20 cm; Esselink and Zwarts, 1989)
456 and *Arenicola Marina* (15-25 cm; Rijken, 1979). Visual evidence of burrows and defaecation
457 mounds suggested the presence of both these species in the bioturbated ponds (Fig. A4,
458 Appendix 4).

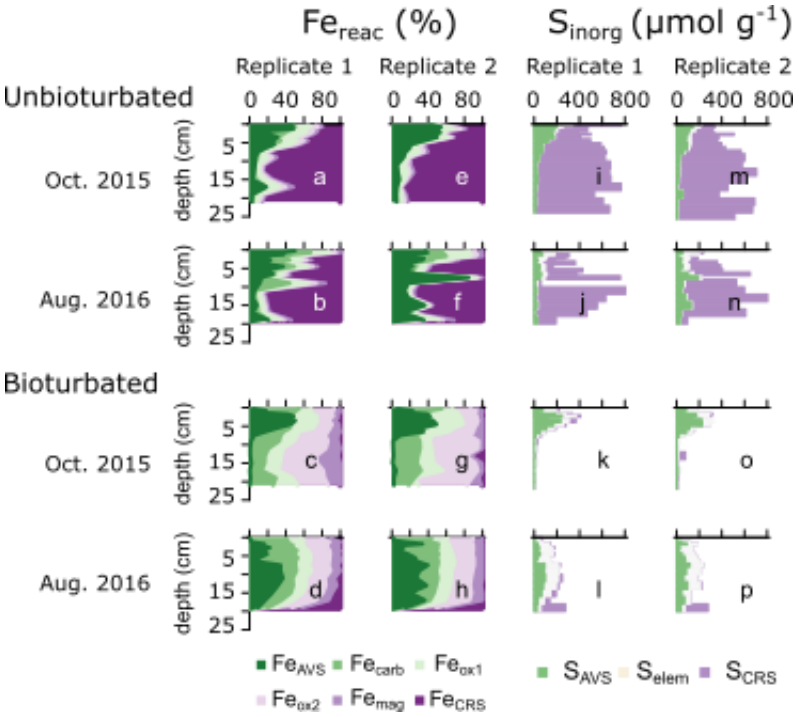

Figure 4: Vertical depth profiles of (a)-(h) reactive iron speciation (Fe_{reac}), (i)-(p) inorganic sulphur speciation (S_{inorg}) recorded in the unbioturbated (upper two rows) and bioturbated ponds (lower two rows) in 2015 and 2016. The results in column one and three are from the same core, while the results in the second and fourth column are also from the same core.

3.5 Pore-water geochemistry

Overall, pore-water profiles for different solutes showed a good correspondence between duplicates and revealed a marked difference between bioturbated and unbioturbated sediments.

In 2015, ammonium (NH_4^+) accumulated with depth in the unbioturbated cores, gradually increasing to a value of 0.8 mM (Fig. 5a). In 2016, NH_4^+ accumulation occurred much faster and showed a subsurface maximum of 1 mM at 6 cm depth, below which NH_4^+ decreased to 0.5-0.8 mM at 20 cm (Fig. 5b). This difference in concentration gradient was reflected in the diffusive fluxes near the SWI; the diffusive flux out of the sediment in 2015 was about 4 times lower than in 2016 (Table 3). In contrast, the bioturbated cores showed limited NH_4^+ accumulation in the first ~2-5 cm, after which the concentrations remained at a low value ~0.2 mM (Fig. 5c,d). This is most likely caused by burrow flushing, which promotes exchange of NH_4^+ with the overlying water, as well as nitrification and the precipitation of metal (Mn) oxides (which can oxidise NH_4^+), by input of oxygen, which limits its accumulation in the pore water.

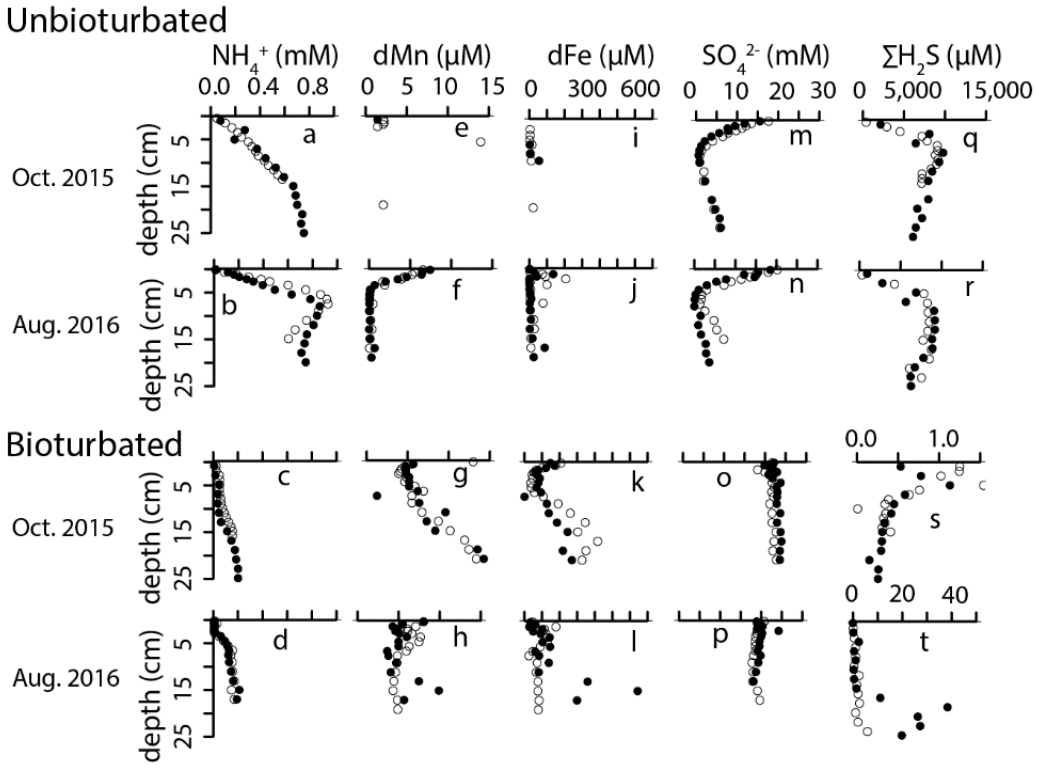

Figure 5: Vertical depth profiles of pore-water solutes collected in 2015 and 2016. Profiles were recorded in the unbioturbated (upper two rows) and bioturbated ponds (lower two rows). (a)-(d) ammonium (NH_4^+), (e)-(h) dissolved manganese (dMn), (i)-(l) dissolved iron (dFe), (m)-(p) Sulphate normalised to chloride (see main text for details) (SO_4^{2-}) and (q)-(t) dissolved free sulphide (ΣH_2S). Note the difference in scale in the ΣH_2S concentration in panels (q) and (r) versus (s) and (t). Filled and open symbols in the same panel indicate replicate cores.

The overall low concentrations of pore-water manganese (dMn) shows that manganese cycling was most likely not important at the field site. Dissolved Mn was undetectable in the unbioturbated cores of 2015 (Fig. 5e, the data point at 5 cm is likely a contamination), and was only present in very low concentrations in the bioturbated cores, where it showed a small decrease from 5 µM to 3 µM at 5 cm, after which dMn increased again to 10 µM (Fig. 5g). The metal samples in 2016 were analysed by HR-ICP-MS, which allowed measurement of dMn and dFe to low concentrations. In the unbioturbated cores, dMn rapidly decreased from 7.5 µM at the SWI to below detection at 4 cm depth (Fig. 5f). In the bioturbated cores, dMn accumulated in the upper 5 cm to ~7.5 µM and decreased to 5 µM below (Fig. 5h).

Depth profiles of dissolved iron showed a good correlation with the dMn profiles; dFe was also undetectable in unbioturbated cores of 2015 (Fig. 5i), while profiles from the bioturbated ponds were similar to dMn, with an initial decrease from 200 µM to ~50 µM in the upper 5 cm, and a subsequent increase to ~300 µM (Fig. 5k). In the unbioturbated cores of 2016, dFe was near the LOQ throughout the core (Fig. 5j). In the bioturbated cores, there was a small enrichment of dFe in the upper 5-10 cm (~200 µM), after which the concentrations dropped to

below the LOQ (Fig. 5l). One replicate showed a peak in dFe concentration at depth, which was also present in the dMn profile (Fig. 5h,l), possibly caused by natural variability.

Sulphate profiles (normalised to Cl^-, see section 2.4) were similar between campaigns in the unbioturbated pond (Fig. 5m,n) and indicated strong sulphate consumption. Diffusive sulphate uptake was calculated on the non-normalised profiles and amounted to 14.6 mmol S m^{-2} d^{-1} in 2015 and 23.7 mmol S m^{-2} d^{-1} in 2016 (Table 3). Sulphate reduction is strongly dependent on temperature (Isaksen and Jørgensen, 1996), and thus the higher temperature in summer (17°C vs 10°C in October; Table 2) could have led to higher sulphate reduction. The increase in sulphate concentration below 10 cm was most likely due to upward diffusion of sulphate from below the sampled depth (there is evidence for a deep hypersaline water source that supplies sulphate from below; Mills et al., 2016). In the bioturbated cores, sulphate profiles were straight (Fig. 5o,p), which suggests that there was no net sulphate consumption, although cryptic sulphur cycling was likely occurring (Mills et al., 2016).

Free sulphide profiles were inversely correlated with the sulphate profiles. Strong sulphate consumption in the unbioturbated cores coincided with high sulphide accumulation (up to 10 mM at 10 cm depth) (Fig.5q,s). Dissolved sulphide fluxes (calculated from the linear gradient in the upper 5-10 cm) were comparable in the unbioturbated cores (19.6 and 17.5 mmol m^{-2} d^{-1}; Table 3), and these were in the same range as the diffusive sulphate uptakes (Table 3). In the bioturbated cores, sulphide concentrations were three orders of magnitude lower (µM range; Fig. 5s,t). The bioturbated core of 2015 showed a little sulphide accumulation (~1.5 µM) in the upper 5 cm, which correlated with the accumulation of inorganic sulphur in the solid phase (Fig. 4k,o and Fig. 5r). In 2016, sulphide concentrations only increased below 15 cm (~30 µM at 20 cm depth) (Fig. 5t).

Table 3: Fluxes at the sediment-water interface (J_{SWI}) and burial fluxes (J_{burial}) of solid-phase species and diffusive fluxes of solutes at the sediment-water interface ($J_{diff,SWI}$) and at the end of the sediment cores ($J_{diff,deep}$). *Diffusive fluxes were estimated based on the average concentration gradient of duplicate cores the same time. Positive fluxes are directed downwards. n.d. = not determined.

Analyte	**Symbol**	**Unit**	**Value**			
			Unbioturbated		*Bioturbated*	
			Oct. 2015	*Aug. 2016*	*Oct. 2015*	*Aug. 2016*
J_{SWI}						
Organic Carbon	POC	mmol C m^{-2} d^{-1}	27 ± 9	18 ± 6	n.d.	n.d.
J_{burial}						
Organic Carbon	POC	mmol C m^{-2} d^{-1}	10 ± 3	12 ± 4	7 ± 2	9 ± 3
Total Nitrogen	TN	mmol N m^{-2} d^{-1}	0.7 ± 0.3	0.8 ± 0.3	0.5 ± 0.2	0.8 ± 0.3
Pyrite	FeS_2	µmol FeS_2 m^{-2} d^{-1}	700 ± 300	400 ± 300	10 ± 8	100 ± 100

Acid volatile sulphide	FeS	µmol FeS m^{-2} d^{-1}	30 ± 10	80 ± 30	5 ± 5	80 ± 40
Elemental Sulphur	S^0	µmol S^0 m^{-2} d^{-1}	3 ± 2	9 ± 5	13 ± 8	140 ± 70
Carbonate iron	Fe_{carb}	µmol Fe m^{-2} d^{-1}	10 ± 10	0	130 ± 70	50 ± 30
Easily reducible iron oxides	Fe_{ox1}	µmol Fe m^{-2} d^{-1}	90 ± 90	40 ± 20	100 ± 100	60 ± 20
Moderately reducible iron oxides	Fe_{ox2}	µmol Fe m^{-2} d^{-1}	40 ± 40	14 ± 6	300 ± 100	120 ± 40
Magnetite iron	Fe_{mag}	µmol Fe m^{-2} d^{-1}	50 ± 40	27 ± 9	90 ± 50	70 ± 20
Total reactive iron	Fe_{reac}	µmol Fe m^{-2} d^{-1}	900 ± 300	600 ± 300	600 ± 200	500 ± 100
$J_{diff,SWI}$ *						
Ammonium	NH_4^+	mmol N m^{-2} d^{-1}	-0.51	-2.01	-0.11	0
Dissolved iron	dFe	mmol Fe m^{-2} d^{-1}	n.d.	-0.3	-0.15	-0.1
Sulphate	SO_4^{2-}	mmol S m^{-2} d^{-1}	14.6	23.7	0	0
Dissolved sulphide	ΣH_2S	mmol S m^{-2} d^{-1}	-19.6	-17.5	-0.001	0
$J_{diff,deep}$ *						
Ammonium	NH_4^+	mmol N m^{-2} d^{-1}	-0.03	0.1	-0.02	-0.03
Dissolved iron	dFe	mmol Fe m^{-2} d^{-1}	n.d.	0	-0.03	0
Sulphate	SO_4^{2-}	mmol S m^{-2} d^{-1}	-1.4	-1.4	0	0
Dissolved sulphide	ΣH_2S	mmol S m^{-2} d^{-1}	1.2	0.6	0	0

4. DISCUSSION

4.1 External inputs and redox dichotomy

Our dataset confirms the redox dichotomy that has previously been observed in the pond sediments of East Anglian salt marshes (Antler et al., 2019; Hutchings et al. (2019). There is iron-rich sediment, characterised by high ferrous iron pore-water concentrations (up to 0.6 mM in the upper 30 cm; Fig. 5k,l) and sulphide-rich sediment, characterised by high pore-water sulphide concentrations (up to 10 mM in the upper 30 cm; Fig. 5q,r). Even though both pond types exhibit seasonal and spatial variability in their chemistry (Figs. 3-5), the differences between iron-rich and sulphide-rich sediments are a clear feature of the East Anglian salt marshes. To explain the origin of the redox dichotomy within these salt marshes (Fig. 1c), Hutchings et al. (2019) carried out an aerial survey of two East Anglian marsh systems. They proposed that a ponds proximity to a creek could potentially determine the pond subsurface geochemistry, with iron-rich ponds tending to be closer to large creeks than sulphide-rich ponds. The spatial positioning would then impose different boundary conditions, which could alter the surface/subsurface delivery of iron and/or the surface delivery of organic carbon (Spivak et al., 2017; Hutchings et al., 2019).

We can test these hypotheses with the current dataset. If a pond receives an increased delivery of dissolved reactive iron, this would also imply that the reactive iron inventory of the iron-rich pond would be systematically higher (as the supply is higher). However, neither the iron speciation (Fig. 3i), nor the estimated burial rates of reactive iron (Table 3), indicate any systematic difference in total reactive iron supply between the two pond types. If anything, the reactive iron burial rates suggest a higher iron supply in the sulphide-rich ponds (Table 3), in contrast to what would be expected (this could also be caused by some lateral diffusional loss from the iron-rich pond sediments to the surrounding soil; Antler et al., 2019). Additionally, solid-phase Fe/Al (Fig. 3o) were very similar between the two pond types, also suggesting that the two pond types are comparable in terms of reactive iron input.

Because of their specific positioning on the marsh, pond types could also potentially differ in the quality and/or quantity of the organic matter they receive. Foremost, a difference in quality is unlikely, as the C:N ratio of organic matter was comparable (~12) in all ponds investigated (Fig. 3f), which suggests that the organic matter source was similar, if not identical, in both pond types. Moreover, the C:N ratio of the salt marsh vegetation surrounding the ponds is considerably higher (18-74; Table 2), suggesting that the sedimentary organic matter was predominantly derived from local growth of marine algae in the ponds (macro-algae and/or microalgae) or from input of suspended marine POC. Pond sediments in temperate salt marsh systems on the US East Coast (MA, USA) have similar C:N ratios (~10), and stable isotope studies have shown most organic carbon is derived from local microalgae growth in the ponds (Spivak et al., 2017; Spivak et al., 2018).

Our data indicate, however, that the quantity of organic matter (Fig. 3c) is significantly different between the two pond type sediments (mean POC 5.1 ± 0.9 % in bioturbated versus 7 ± 2 % in unbioturbated). To analyse the cause of this difference, we establish a simple mass budget for organic carbon and obtain a relation for the key factors that control the magnitude of the mean POC ($\hat{C}$) (see Appendix 2 for the full derivation)

$$\hat{C} = \frac{J_{input}}{\left(kL + \nu_{sed}\right)} \qquad [6]$$

where J_{input} is the input flux of organic carbon, ν_{sed} is the sedimentation velocity, k is the first-order degradation constant, and L is the depth of the sediment interval. Our radionuclide data indicate that the sedimentation velocity ν_{sed} is 0.3 cm yr^{-1}, and that it is similar in both the bioturbated and unbioturbated ponds (see section 3.2). So, if the mean POC is lower in the bioturbated ponds, Eq. [6] implies that either the organic input J_{input} is lower in the bioturbated

ponds, or that the intrinsic mineralisation rate k must be greater in the presence of burrowing fauna (or a combination of both).

We contend that a stimulation of organic matter mineralisation by fauna is a more likely explanation than a differential input of organic matter. If we assume that differential organic matter input alone is the cause of the concentration difference, then equation [6] predicts that the POC input into unbioturbated ponds should be ~37% higher than in bioturbated ponds (Appendix 2). The estimated organic matter input in the unbioturbated ponds is 13 - 50 mmol C m^{-2} d^{-1} (see Appendix 2 for the calculations). A 37% decrease is substantial and would lead to reduced mineralisation rates in the bioturbated ponds (Fig. 6a,b). Such a big difference in POC input would also be difficult to reconcile with the proximity of both types of ponds on the marsh. Instead, we advance that the differences observed within the ponds are mainly related to the presence of bioturbating fauna. If we assume that organic matter input in both ponds types is the same, and that the observed difference in POC concentrations solely results from the presence of the burrowing macrofauna, then bioturbation could stimulate the rate of organic matter mineralisation by 12-33 % (Fig. 6c,d; Appendix 2). Previous laboratory incubation studies have estimated increases in mineralisation rates due to bioturbation from 50 % to 275 % (Kristensen et al., 1992; Banta et al., 1999; Bianchi et al., 2000; Heilskov and Holmer, 2001; Papaspyrou et al., 2007; Papaspyrou et al., 2010; Nascimento et al., 2012). These values are higher than our estimate and are likely an overestimation of the effects observed in the field (Welsh, 2003), suggesting that the observed decrease in POC could well be due to macrofauna.

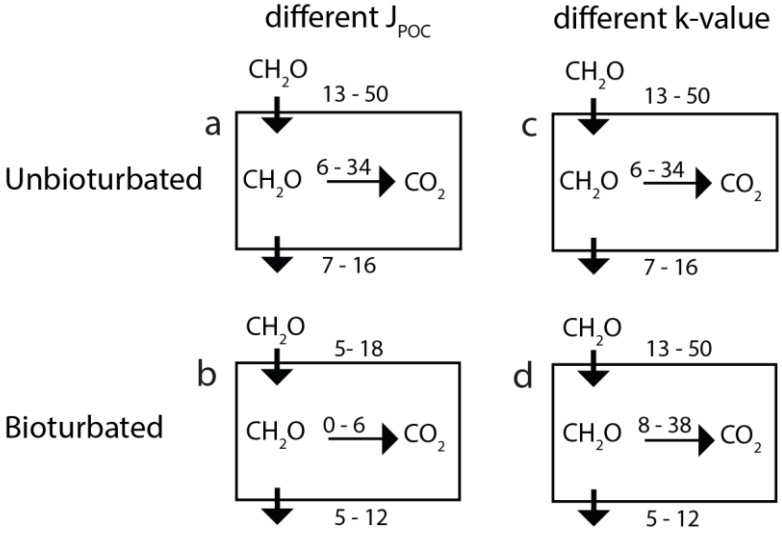

Figure 6: A rudimentary mass budget for organic carbon, following equation [6]. All fluxes in mmol C m^{-2} d^{-1}. See main text and Appendix 2 for details.

4.2 Bioturbation stimulates iron and sulphur recycling

To better understand the redox dichotomy observed in the pond sediments, we have constructed an early diagenetic 'ideal world' model based on our field observations (Appendix 1) to compare two sediment columns, one without and one with bioturbation (Figure 7). We use these model results to qualitatively illustrate the effect of bioturbation on the depth profiles of key iron (Fe^{2+} and FeOOH) and sulphur species (SO_4^{2-} and ΣH_2S). Additionally, we have compiled quantitative estimates of Fe and S cycling numbers (the number of times an element cycles between its oxidised and reduced state; Eq. [5]) in bioturbated and unbioturbated sediments from the literature (Table 4). Note that these modelling results assume that the sediment columns are in steady state, which is likely not the case for our salt marsh system. Nevertheless, this modelling exercise does help to illustrate the impact of bioturbating fauna on sedimentary Fe-S cycling.

In an unbioturbated sediment, the diagenetic model predicts that organic matter mineralisation is driven by sulphate reduction (leading to SO_4^{2-} depletion; Fig. 7d), while FeOOH is directly transformed to FeS and FeS_2 (Fig. 7a) and dissimilatory iron reduction is suppressed. As a result, free sulphide builds up to high concentrations in the pore water (Fig. 7d), while ferrous iron (Fe^{2+}) remains low (Fig. 7b). These same features are seen in our field pore-water data from the unbioturbated sediment (Fig. 5). Overall, an unbioturbated sediment is characterized by low levels of Fe and S recycling. The trapping of Fe(II) as $FeS_{(2)}$ limits its upward diffusion to the oxic zone, and thus inhibits its re-oxidation by oxygen, nitrate or manganese oxides, which restricts the internal Fe recycling (Widerlund and Ingri, 1996). Similarly, the absence of biomixing implies that FeS and FeS_2 are not transported back into the oxic zone. This should limit the re-oxidation of reduced sulphide and hence reduce the S recycling. While field studies suggest no Fe and S recycling in unbioturbated sediments (N_S ~ N_{Fe} ~1; Table 4), model simulations do predict higher cycling numbers (N_S ~ 5-6; N_{Fe} ~10; Table 4). According to the diagenetic model, some iron and sulphur recycling must occur within a narrow zone around the oxic-anoxic transition in the sediment (Fig. A5, Appendix 4; van de Velde and Meysman, 2016). As this recycling occurs within a very narrow zone (micrometres), it is very difficult to capture this process with the current core slicing procedures and analytical measurements. More fine-scaled measurement methods (e.g., high resolution voltammetric micro-electrode measurements or diffusive gradient in thin film methods; Anschutz et al., 2000; Gao et al., 2015) should investigate whether this cycling is a model artefact, or a genuine process occurring in the sediment.

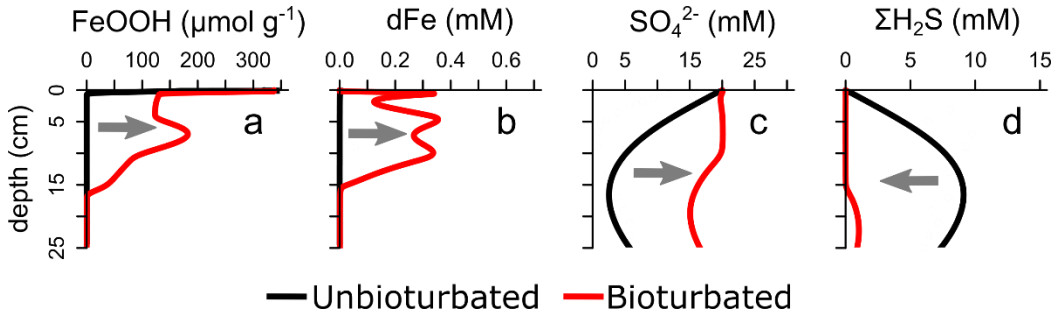

Figure 7: Model results of two identical sediments, one without bioturbation (black line) and one with bioturbation (red line). Model set-up is described in Appendix 1, model scenario shown here is 'B + SP' and an irrigation rate of 1.2 yr^{-1}. (a) iron oxide (FeOOH), (b) dissolved iron (dFe), (c) sulphate (SO_4^{2-}), (d) free sulphide (HS^-). Grey arrow indicates the effect of bioturbation; the sediment becomes higher in iron content due to the stimulation of iron cycling, which limits the build-up of free sulphide.

The inclusion of bioturbation in the model substantially alters the biogeochemical cycling within the sediment (Figure 7). The in-flushing of O_2 through bio-irrigation sustains high concentrations of iron oxides in the upper 10 cm (Fig. 7a), consistent with our field observations (Figure 4a-h), and allows the build-up of dissolved Fe(II) in the pore water (Fig. 5k,l, Fig. 7a). Overall, bioturbated sediments are characterized by elevated levels of Fe and S recycling (Table 4; van de Velde and Meysman, 2016). Bio-mixing results in an upward transport of FeS to the oxic zone and its oxidative dissolution (Canfield et al., 1993; Thamdrup et al., 1994), while bio-irrigation creates an additional influx of O_2 at depth, which also triggers the oxidation of free sulphide and ferrous iron (Berner and Westrich, 1985; Aller and Aller, 1998). Both model studies and field assessments show that N_{Fe} and N_S values are substantially higher in bioturbated than in unbioturbated sediments (Table 4).

Overall, the inclusion of bioturbation in the diagenetic model generates a transition from a sulphur-dominated to an iron-dominated sediment (Fig. 7), which closely reproduces the dichotomy that is seen in our field data (Fig. 5). By stimulating Fe recycling, bioturbation limits the accumulation of free sulphide in the pore water (Figure 7d), and promotes the accumulation of ferrous iron. As a result, the sediment changes from a sulphur-dominated systems to an iron-dominated system (Figure 7), consistent with our field observations (Fig. 5).

Element		Cycling number	Reference
Fe - unbioturbated	*Field data*	1	(Widerlund and Ingri, 1996)
	Modelling	10	(van de Velde and Meysman, 2016)
Fe - bioturbated	*Field data*	4 - 21	(Thibault de Chanvalon et al., 2017)
	"	1 – 2.5	(Slomp et al., 1997)

	″	15	(Thamdrup et al., 1994)
	″	130 - 300	(Canfield et al., 1993)
	″	8	(Krom et al., 2002)
	″	4 - 453	(Esch et al., 2013)
	Modelling	40	(van de Velde and Meysman, 2016)
	″	9	(Wijsman et al., 2001)
	″	9 - 13	(Van Cappellen and Wang, 1996)
S - unbioturbated	*Field data*	1 – 3	(Middelburg, 1991)
	″	1 – 4	(Berner and Westrich, 1985)
	″	1	(Chanton et al., 1987)
	Global estimate	1 – 5	(Canfield and Farquhar, 2009)
	Modelling	5 – 6	(van de Velde and Meysman, 2016)
S - bioturbated	*Field data*	10	(Jørgensen, 1977)
	″	7 – 17	(Berner and Westrich, 1985)
	″	17	(Chanton et al., 1987)
	″	59	(Fallon, 1987)
	″	17	(Swider and Mackin, 1989)
	Global estimate	33	(Canfield and Farquhar, 2009)
	Modelling	10	(van de Velde and Meysman, 2016)

Table 4: Literature estimations of cycling numbers for Fe and S. See Eq. [5] for how cycling numbers have been calculated.

4.3 Alternative stable states in iron-sulphur cycling

We have shown that the differences in input fluxes between pond types are likely small (section 4.1), so that these cannot act as the direct drivers of the observed redox dichotomy (large differences in redox chemistry would require large variations in solid-phase carbon and iron inputs). Instead, our results suggest that the presence/absence of bioturbation is the driving force behind the observed dichotomy in redox chemistry (section 4.2). Note, however, that this does not fully resolve the "redox dichotomy" conundrum. It simply replaces the old question (how can ponds only meters apart have a completely different redox chemistry?) with a new one (how can ponds only meters apart have completely different bioturbation conditions?).

We propose that the key lies in the close interplay between the early diagenetic cycles of iron and sulphur, small differences in solid-phase inputs and the superimposed effect of bioturbation on the coupled Fe-S cycles. We advance that non-linear interactions in the Fe-S cycles can generate alternative stable states, in which small differences in inputs can be amplified by positive feedbacks. The general scheme of how such alternative stable states can be generated is depicted in Figure 8. The positive feedback loop starts with the fact that free sulphide is generally toxic to animals and the accumulation of free sulphide in the pore water would inhibit the colonisation of the sediment by fauna. Less fauna implies less bioturbation. Hence, as discussed above, this increases the importance of sulphate reduction relative to dissimilatory iron reduction, leading to high amounts of free sulphide in the pore water (Figure 7a), which then excludes bioturbation, limits the internal recycling of Fe and reinforces the

accumulation of free sulphide. Altogether this provides a positive feedback (Figure 8a), and the presence of such feedbacks has been demonstrated to generate alternative stable states in a range of natural systems, including the P cycling in shallow lakes and diatom growth in coastal systems (Van de Koppel et al., 2001; Carpenter, 2005).

By means of a positive feedback, a small initial perturbation in the sedimentary redox state of the ponds can be amplified, promoting a chemistry flip either to an S-dominated or an Fe-dominated state (Figure 8b). For example, one can imagine a scenario in which a small disturbance occurs and less organic matter arrives at the sediment (e.g. the pond is flushed just before winter and the algae biomass in the overlying water is removed). Following that disturbance, less sulphide will be produced in the pore water. This may allow some burrowing faunal species to colonise the sediment, which then stimulates the redox recycling of Fe within the sediment, thus reducing free sulphide concentrations and improving the living conditions for other macrofauna. The pond would then rapidly evolve to a Fe-dominated redox state. Alternatively, if the pond initially received an elevated input of organic matter, sulphide would accumulate in the pore water, preventing the colonisation of burrowing fauna. This would reduce the redox recycling of Fe within the sediment, stimulating the accumulation of free sulphide to higher levels, which keep out bioturbators. In this way, for near-identical boundary conditions, one can thus have two contrasting redox conditions.

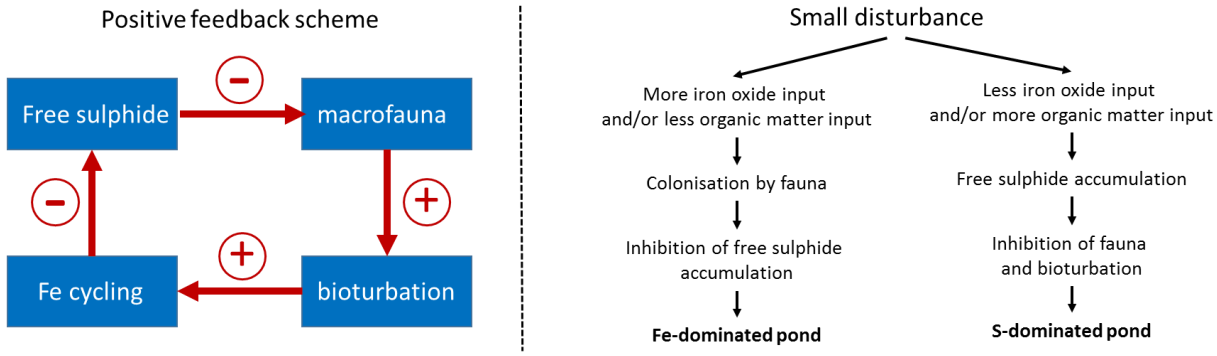

Figure 8: (a) Proposed mechanism for a positive feedback in Fe/S cycling in salt marsh ponds (b) Proposed sequence of events leading to the observed sedimentary redox dichotomy in salt marsh ponds.

5. SUMMARY, CONCLUSIONS AND OUTLOOK

Bioturbation has a major impact on the redox cycling of carbon, iron and sulphur in aquatic sediments. We compared two identical sedimentary settings, where the main difference was the presence of bioturbation. Based on *in-situ* observations, we have shown that bioturbation stimulates organic matter mineralisation by 12-33 %. The presence of burrowing of marine

fauna also stimulated iron cycling at the expense of sulphur cycling. Overall, our results illustrated how the presence of burrowing fauna drives the sedimentary redox chemistry from a sulphide-dominated state to an iron-dominated state.

The salt marsh complexes along the East Anglian (UK) coast are characterised by an intriguing redox dichotomy. Pond sediments can be classified either as sulphide-dominated and unbioturbated or iron-dominated and bioturbated. We have shown that the presence or absence of bioturbators are the likely driving force behind the observed redox dichotomy in the salt marsh complexes. We propose that the seemingly random distribution of bioturbated and unbioturbated ponds is caused by small differences in solid-phase inputs and the non-linear interactions in the coupled Fe-S cycles, which can generate alternative stable states, in which small differences in inputs can be amplified by positive feedbacks. To test this hypothesis further, an in-depth model analysis of the coupled cycles of carbon, iron and sulphur in marine sediments is required. Moreover, the strong non-linear interaction between iron and sulphur cycling is not a specific feature of salt marsh sediments, but applies to many more types of marine sediments, and hence suggests that alternative stable states in redox cycling could also be present in other marine systems.

6. ACKNOWLEDGEMENTS

The research leading to these results was financially supported by the Belgian American Educational Foundation (postdoctoral fellowship to SVDV) and the Research Foundation Flanders (PhD fellowship to SVDV). FJRM was financially supported by the European Research Council under the European Union's Seventh Framework Program (FP/2007-2013) through ERC Grant 306933, by the Research Foundation Flanders via FWO grant G031416N, and the Netherlands Organization for Scientific Research (VICI grant 016.VICI.170.072). The HR-ICP-MS instrument was financed by the HERCULES Foundation (Code: UABR/11/010). The authors would like to thank Jurian Brasser, Peter Van Breugel, Jan Sinke, Jan Peene, Yvonne van der Maas, Pieter Van Rijswijk of NIOZ Yerseke and David Verstraeten of the Vrije Universiteit Brussel for the analysis of the pore-water and sediment samples. Additionally, we would like to thank Kirsten Imhoff and Timothy F. Ferdelman from the Max Planck Institute for Marine Microbiology for the analysis of the elemental sulphur samples.

7. References

Aller R. C. (2014) Sedimentary Diagenesis, Depositional Environments, and Benthic Fluxes. In *Treatise on Geochemistry (2nd ed.)* Elsevier Ltd. pp. 293–334. Available at: http://dx.doi.org/10.1016/B978-0-08-095975-7.00611-2.

Aller R. C. (1977) The influence of macrobenthos on chemical diagenesis of marine sediments. Yale University.

Aller R. C. and Aller J. Y. (1998) The effect of biogenic irrigation intensity and solute exchange on diagenetic reaction rates in marine sediments. *J. Mar. Res.* **56**, 905–936.

Aminot A., Kérouel R. and Coverly S. C. (2009) Nutrients in seawater using segmented flow analysis. In *Practical guidelines for the analysis of seawater* (ed. O. Wurl). CRC press.

Anschutz P., Sundby B., Lefrançois L., Luther G. W. and Mucci A. (2000) Interactions between metal oxides and species of nitrogen and iodine in bioturbated marine sediments. *Geochim. Cosmochim. Acta* **64**, 2751–2763.

Antler G., Mills J. V., Huthings A., Redeker K. and Turchyn A. V. (2019) The sedimentary carbon-sulfur-iron interplay - a lesson from East Anglian salt marsh sediments. *Front. Earth Sci.* **7**, 140.

Appleby P. G. and Oldfield F. (1978) The calculation of lead-210 dates assuming a constant rate of supply of unsupported 210Pb to the sediment. *Catena* **5**, 1–8.

Archer D. and Devol A. H. (1992) Benthic oxygen fluxes on the Washington shelf and slope: A comparison of in situ microelectrode and chamber flux measurements. *Limnol. Oceanogr.* **37**, 614–629.

Banta G. T., Holmer M., Jensen M. H. and Kristensen E. (1999) Effects of two polychaete worms, Nereis diversicolor and Arenicola marina, on aerobic and anaerobic decomposition in a sandy marine sediment. *Aquat. Microb. Ecol.* **19**, 189–204.

Berner R. A. and Westrich J. T. (1985) Bioturbation and the early diagenesis of carbon and sulfur. *Am. J. Sci.* **285**, 193–206.

Bianchi T. S., Johansson B. and Elmgren R. (2000) Breakdown of phytoplankton pigments in Baltic sediments: Effects of anoxia and loss of deposit-feeding macrofauna. *J. Exp. Mar. Bio. Ecol.* **251**, 161–183.

Boudreau B. P. (1997) *Diagenetic Models and their Implementation*., Springer-Verlag Berlin Heidelberg New York.

Boudreau B. P. (1996) The diffusive tortuosity of fine-grained unlithified sediments. *Geochim. Cosmochim. Acta* **60**, 3139–3142.

Boudreau B. P., Mucci A., Sundby B., Luther III G. W. and Silverberg N. (1998) Comparative diagenesis at three sites on the Canadian continental margin. *J. Mar. Res.* **56**, 1259–1284.

Canfield D. E. and Farquhar J. (2009) Animal evolution, bioturbation, and the sulfate concentration of the oceans. *Proc. Natl. Acad. Sci.* **106**, 8123–8127.

Canfield D. E., Raiswell R., Westrich J. T., Reaves C. M. and Berner R. a. (1986) The use of chromium reduction in the analysis of reduced inorganic sulfur in sediments and shales. *Chem. Geol.* **54**, 149–155.

Canfield D. E., Thamdrup B. and Hansen J. W. (1993) The anaerobic degradation of organic matter in Danish coastal sediments: iron reduction, manganese reduction, and sulfate reduction. *Geochim. Cosmochim. Acta* **57**, 3867–3883.

Van Cappellen P. and Wang Y. (1996) Cycling of iron and manganese in surface sediments: a general theory for the coupled transport and reaction of carbon, oxygen, nitrogen, sulfur, iron, and manganese. *Am. J. Sci.* **296**, 197–243.

Carpenter S. R. (2005) Eutrophication of aquatic ecosystems: Bistability and soil phosphorus. *Proc. Natl. Acad. Sci.* **102**, 10002–10005.

Chanton J. P., Martens C. S. and Goldhaber M. B. (1987) Biogeochemical cycling in an organic-rich coastal marine basin. 7. Sulfur mass balance, oxygen uptake and sulfide retention. *Geochim. Cosmochim. Acta* **51**, 1187–1199.

Cline J. D. (1969) Spectrophotometric Determination of Hydrogen Sulfide in Natural Waters. *Limnol. Oceanogr.* **14**, 454–458.

Cornwell J. C. and Morse J. W. (1987) The characterization of iron sulfide minerals in anoxic sediments. *Mar. Chem.* **22**, 193–206.

Crompton T. R. (1989) Metals. In *Analysis of Seawater* Butterworths & Co. pp. 74–215.
Dickson A. G., Afghan J. D. and Anderson G. C. (2003) Reference materials for oceanic CO2 analysis: a method for the certification of total alkalinity. *Mar. Chem.* **80**, 185–197. Available at: http://www.sciencedirect.com/science/article/pii/S0304420302001330.
Elrod V. A., Berelson W. M., Coale K. H. and Johnson K. S. (2004) The flux of iron from continental shelf sediments: A missing source for global budgets. *Geophys. Res. Lett.* **31**, 2–5.
Esch M. E. S., Shull D. H., Devol A. H. and Moran S. B. (2013) Regional patterns of bioturbation and iron and manganese reduction in the sediments of the southeastern Bering Sea. *Deep. Res. Part II Top. Stud. Oceanogr.* **94**, 80–94. Available at: http://dx.doi.org/10.1016/j.dsr2.2013.04.004.
Esselink P. and Zwarts L. (1989) Seasonal trend in burrow depth and tidal variation in feeding activity of Nereis diversicolor. *Mar. Ecol. Prog. Ser.* **56**, 243–254.
Fallon R. D. (1987) Sedimentary sulfides in the Nearshore Georgia Bight. *Estuar. Coast. Shelf Sci.* **25**, 607–619.
French J. R. (1993) Numerical simulation of vertical marsh growth and adjustment to accelerated sea-level rise, North Norfolk, U.K. *Earth Surf. Process. Landforms* **18**, 63–81.
Funnell B. and Pearson I. (1989) Holocene sedimentation on the North Norfolk barrier coast in relation to relative sea-level change. *J. Quat. Sci.* **4**, 25–36.
Gao Y., van de Velde S., Williams P. N., Baeyens W. and Zhang H. (2015) Two-dimensional images of dissolved sulfide and metals in anoxic sediments by a novel diffusive gradients in thin film probe and optical scanning techniques. *TrAC - Trends Anal. Chem.* **66**.
Gros N., Camões M. F., Oliveira C. and Silva M. C. R. (2008) Ionic composition of seawaters and derived saline solutions determined by ion chromatography and its relation to other water quality parameters. *J. Chromatogr. A* **1210**, 92–8. Available at: http://www.ncbi.nlm.nih.gov/pubmed/18829032 [Accessed December 3, 2014].
Heilskov A. C. and Holmer M. (2001) Effects of benthic fauna on organic matter mineralization in fish-farm sediments: importance of size and abundance. *ICES J. Mar. Sci.* **58**, 427–434.
Hutchings A. M., Antler G., Wilkening J., Basu A., Bradbury H. J., Clegg J. A., Gorka M., Lin C. Y., Mills J. V., Pellerin A., Redeker K., Sun X. and Turchyn A. V. (2019) Creek dynamics determine pond subsurface geochemical heterogeneity in East Anglian (UK) salt marshes. *Front. Earth Sci.* **7**, 41. Available at: https://www.frontiersin.org/articles/10.3389/feart.2019.00041/abstract [Accessed March 6, 2019].
Isaksen M. F. and Jørgensen B. O. B. (1996) Adaptation of psychrophilic and psychrotrophic sulfate-reducing bacteria to permanently cold marine environments. *Appl. Environ. Microbiol.* **62**, 408–414.
Jones C. G., Lawton J. H. and Shachak M. (1994) Organisms as Ecosystem Engineers. *Oikos* **69**, 373–386.
Jørgensen B. B. (1977) The sulfur cycle of a coastal marine sediment (Limfjorden). *Limnol. Oceanogr.* **22**, 814–832.
Kallmeyer J., Ferdelman T. G., Weber A., Fossing H. and Jørgensen B. B. (2004) Evaluation of a cold chromium distillation procedure for recovering very small amounts of radiolabeled sulfide related to sulfate reduction measurements. *Limnol. Oceanogr. Methods* **2**, 171–180.
Kamyshny A., Borkenstein C. G. and Ferdelman T. G. (2009) Protocol for Quantitative Detection of Elemental Sulfur and Polysulfide Zero-Valent Sulfur Distribution in Natural

840 Aquatic Samples. *Geostand. Geoanalytical Res.* **33**, 415–435. Available at:
841 http://doi.wiley.com/10.1111/j.1751-908X.2009.00907.x [Accessed May 28, 2019].
842 Van de Koppel J., Herman P. M., Thoolen P. and Heip C. H. (2001) Do alternate stable states
843 occur in natural ecosystems? Evidence from a tidal flat. *Ecology* **82**, 3449–3461.
844 Available at: https://www.jstor.org/stable/pdf/2680164.pdf [Accessed May 15, 2019].
845 Kostka J. E., Gribsholt B., Petrie E., Dalton D., Skelton H. and Kristensen E. (2002) The rates
846 and pathways of carbon oxidation in bioturbated saltmarsh sediments. *Limnol.*
847 *Oceanogr.* **47**, 230–240.
848 Kostka J. E. and Luther III G. W. (1994) Partitioning and speciation of solid phase iron in
849 saltmarsh sediments. *Geochim. Cosmochim. Acta* **58**, 1701–1710.
850 Kristensen E., Andersen F. and Blackburn T. H. (1992) Effects of benthic macrofauna and
851 temperature on degradation macroalgal detritus: The fate of organic carbon. *Limnol.*
852 *Oceanogr.* **37**, 1404–1419.
853 Kristensen E., Penha-Lopes G., Delefosse M., Valdemarsen T., Quintana C. O. and Banta G.
854 T. (2012) What is bioturbation? the need for a precise definition for fauna in aquatic
855 sciences. *Mar. Ecol. Prog. Ser.* **446**, 285–302.
856 Krom M. D., Mortimer R. J. G., Poulton S. W., Hayes P., Davies I. M., Davison W. and
857 Zhang H. (2002) In-situ determination of dissolved iron production in recent marine
858 sediments. *Aquat. Sci.* **64**, 282–291. Available at:
859 http://www.scopus.com/inward/record.url?eid=2-s2.0-
860 0036438897&partnerID=tZOtx3y1.
861 Lecroart P., Maire O., Schmidt S., Grémare A., Anschutz P. and Meysman F. J. R. (2010)
862 Bioturbation, short-lived radioisotopes, and the tracer-dependence of biodiffusion
863 coefficients. *Geochim. Cosmochim. Acta* **74**, 6049–6063.
864 McCave I. . N. (1986) Evaluation of a laser-diffraction-size analyzer for use with natural
865 sediments. *J. Sediment. Res.* **54**, 561–564.
866 McLennan S. M. (2001) Relationships between the trace element composition of sedimentary
867 rocks and upper continental crust. *Geochemistry, Geophys. Geosystems* **2**.
868 Meysman F. J. R., Boudreau B. P. and Middelburg J. J. (2005) Modeling reactive transport in
869 sediments subject to bioturbation and compaction. *Geochim. Cosmochim. Acta* **69**, 3601–
870 3617. Available at: http://linkinghub.elsevier.com/retrieve/pii/S0016703705000499
871 [Accessed January 27, 2014].
872 Meysman F. J. R., Middelburg J. J. and Heip C. H. R. (2006) Bioturbation: a fresh look at
873 Darwin's last idea. *Trends Ecol. Evol.* **21**, 688–95. Available at:
874 http://www.ncbi.nlm.nih.gov/pubmed/16901581 [Accessed January 20, 2014].
875 Middelburg J. J. (1991) Organic carbon, sulphur, and iron in recent semi-euxinic sediments of
876 Kau Bay, Indonesia. *Geochim. Cosmochim. Acta* **55**, 815–828.
877 Mills J. V., Antler G. and Turchyn A. V. (2016) Geochemical evidence for cryptic sulfur
878 cycling in salt marsh sediments. *Earth Planet. Sci. Lett.* **453**, 23–32.
879 Nascimento F. J. a., Naslund J. and Elmgren R. (2012) Meiofauna enhances organic matter
880 mineralization in soft sediment ecosystems. *Limnol. Oceanogr.* **57**, 338–346. Available
881 at:
882 http://apps.webofknowledge.com/full_record.do?product=UA&search_mode=GeneralSe
883 arch&qid=6&SID=Y1AFLh5bIFOEdknDAF2&page=1&doc=1.
884 Nieuwenhuize J., Maas Y. E. M. and Middelburg J. J. (1994) Rapid analysis of organic
885 carbon and nitrogen in particulate materials. *Mar. Chem.* **45**, 217–224.
886 Papaspyrou S., Kristensen E. and Christensen B. (2007) Arenicola marina (Polychaeta) and
887 organic matter mineralisation in sandy marine sediments: in situ and microcosm
888 comparison. *Estuar. Coast. Shelf Sci.* **72**, 213–222.
889 Papaspyrou S., Thessalou-Legaki M. and Kristensen E. (2010) The influence of infaunal

(Nereis diversicolor) abundance on degradation of organic matter in sandy sediments. *J. Exp. Mar. Bio. Ecol.* **393**, 148–157.
Pethick J. (1980) the Holocene transgression : initiation during the example of the North Norfolk marshes, England. *J. Biogeogr.* **7**, 1–9.
Pethick J. S. (1974) The distribution of salt pans on tidal salt marshes. *J. Biogeogr.* **1**, 57–62.
Poulton S. W. and Canfield D. E. (2005) Development of a sequential extraction procedure for iron: Implications for iron partitioning in continentally derived particulates. *Chem. Geol.* **214**, 209–221.
Pye K., Dickson J. A. D., Schiavon N., Coleman M. L. and Cox M. (1990) Formation of siderite-Mg-calcite-iron sulphide concretions in intertidal marsh and sandflat sediments, north Norfolk, England. *Sedimentology* **37**, 325–343.
Raiswell R. and Canfield D. E. (2012) The Iron Biogeochemical Cycle Past and Present. *Geochemical Perspect.* **1**, 1–232.
Rijken M. (1979) Food and food uptake in Arenicola Marina. *Netherlands J. Sea Res.* **13**, 406–421.
Robbins J. A., McCall P. L., Berton Fisher J. and Krezoski J. R. (1979) Effect of deposit Feeders on migration of 137CS in lake sediments. *Earth Planet. Sci. Lett.* **42**, 277–287. Available at: https://www.degruyter.com/view/books/9783110490831/9783110490831-001/9783110490831-001.xml.
Sanchez-Cabeza J. A., Ani-Ragolta I. and Masquè P. (2000) Some considerations of the ^{210}Pb constant rate of supply (CRS) dating model. *Limnol. Oceanogr.* **45**, 990–995. Available at: http://doi.wiley.com/10.4319/lo.2000.45.4.0990.
Sanchez-Cabeza J. A. and Ruiz-Fernández A. C. (2012) 210Pb sediment radiochronology: An integrated formulation and classification of dating models. *Geochim. Cosmochim. Acta* **82**, 183–200.
Slomp C. P., Malschaert J. F. P., Lohse L. and Van Raaphorst W. (1997) Iron and manganese cycling in different sedimentary environments on the North Sea continental margin. *Cont. Shelf Res.* **17**, 1083–1117.
Soetaert K., Petzoldt T. and Meysman F. J. R. (2010) marelac: Tools for Aquatic Sciences R package version 2.1.
Spivak A. C., Gosselin K., Howard E., Mariotti G., Forbrich I., Stanley R. and Sylva S. P. (2017) Shallow ponds are heterogeneous habitats within a temperate salt marsh ecosystem. *J. Geophys. Res. Biogeosciences* **122**, 1371–1384. Available at: http://doi.wiley.com/10.1002/2017JG003780 [Accessed March 6, 2018].
Spivak A. C., Gosselin K. M. and Sylva S. P. (2018) Shallow ponds are biogeochemically distinct habitats in salt marsh ecosystems. *Limnol. Oceanogr.* **63**, 1622–1642.
Swider K. T. and Mackin J. E. (1989) Transformations of sulfur compounds in marsh-flat sediments. *Geochim. Cosmochim. Acta* **53**, 2311–2323.
Thamdrup B., Fossing H. and Jorgensen B. B. (1994) Manganese, iron, and sulfur cycling in a coastal marine sediment, Aarhus Bay, Denmark. *Geochim. Cosmochim. Acta* **58**, 5115–5129.
Thibault de Chanvalon A., Metzger E., Mouret A., Knoery J., Geslin E. and Meysman F. J. R. (2017) Two dimensional mapping of iron release in marine sediments at submillimetre scale. *Mar. Chem.* **191**, 34–49. Available at: http://dx.doi.org/10.1016/j.marchem.2016.04.003.
van de Velde S. and Meysman F. J. R. (2016) The influence of bioturbation on iron and sulphur cycling in marine sediments: a model analysis. *Aquat. Geochemistry* **22**, 469–504.
van de Velde S., Mills B., Meysman F. J., Lenton T. M. and Poulton S. W. (2018) Early Palaeozoic ocean anoxia and global warming driven by the evolution of shallow

940 burrowing. *Nat. Commun.* **9**, 2554.
941 Welsh D. T. (2003) It's a dirty job but someone has to do it: The role of marine benthic
942 macrofauna in organic matter turnover and nutrient recycling to the water column. *Chem.*
943 *Ecol.* **19**, 321–342. Available at:
944 http://www.tandfonline.com/doi/abs/10.1080/0275754031000155474.
945 Widerlund A. and Ingri J. (1996) Redox Cycling of Iron and Manganese in Sediments of the
946 Kalix River Estuary, Northern Sweden. *Aquat. Geochemistry* **2**, 185–201.
947 Wijsman J. W. M., Middelburg J. J. and Heip C. H. R. (2001) Reactive iron in Black Sea
948 Sediments: Implications for iron recycling. *Mar. Geol.* **172**, 167–180.
949

Appendix 1: Diagenetic model formulation

Biogeochemical Model Formulation

The biogeochemical model description follows the standard approach to describe reactive transport in marine sediment and comprises a conventional early diagenetic model (Boudreau, 1997; Berg et al., 2003; Meysman et al., 2003). The core of this reactive transport model consists of a set of mass balance equations of the advection-diffusion-reaction form (Boudreau, 1997; Meysman et al., 2005). Adopting the assumption of steady-state compaction, the balance equation for a pore-water solute and solid components becomes (Meysman et al., 2005):

$$\begin{aligned} \phi_F \frac{\partial C_i}{\partial t} &= \frac{\partial}{\partial x}\left[\phi_F D_i \frac{\partial C_i}{\partial x} - \phi_F^{\infty} v_F C_i \right] + \phi_F \alpha_i \left(C_i^{OW} - C_i \right) + \sum_k \nu_{i,k} R_k \\ \phi_S \frac{\partial S_j}{\partial t} &= \frac{\partial}{\partial x}\left[\phi_S D_B \frac{\partial S_j}{\partial x} - \phi_S^{\infty} v_S S_j \right] + \sum_k \nu_{j,k} R_k \end{aligned} \qquad [1]$$

The quantity C_i represents the concentration of a pore-water compound, C_i^{OW} is the value in the overlying water, ϕ_F denotes the porosity (implemented via an exponentially decreasing depth relation as described below), ϕ_F^{∞} is the asymptotic porosity at depth, D_i is the diffusion coefficient, and v_F is the burial velocity of the pore fluids. The solid volume fraction is calculated from porosity (ϕ_S=1-ϕ_F) and v_S is the burial velocity of the solids. The concentration S_j of a solid compound is expressed per unit volume of solid sediment. The quantities R_k represent the rates of the biogeochemical reactions (expressed per bulk sediment volume), where $\nu_{i,k}$ is the stoichiometric coefficient of the *i*-th species in the *k*-th reaction.

Transport parameters

The model includes four different transport parameters; (i) molecular diffusion, (ii) downward advection as a consequence of burial, (iii) bio-mixing and (iv) bio-irrigation. The solute flux due to molecular diffusion and advection is described by Fick's first law (Fick, 1855),

$$J_D = -\phi D_i \frac{\partial C_i}{\partial z} + \phi \nu C_i \qquad [2]$$

where the molecular diffusion coefficient D_i^{mol} is first calculated as a function of temperature and salinity using the CRAN:marelac package (Soetaert et al., 2010a) and corrected for

tortuosity according to the modified Wiessberg relation of Boudreau (1996), i.e., $D_i = D_i^{mol} / (1 - 2\ln\phi_F)$. The model adopts a constant sediment accumulation rate F_{sed} = 0.10 g cm^{-2} yr^{-1}, determined from core dating (see main text). An exponential declining porosity profile was imposed,

$$\phi_F = \phi_F^0 + (\phi_F^0 - \phi_F^\infty) e^{-z/x_{att}} \quad [3]$$

where φ_F^0 is 0.96, φ_F^∞ is 0.78 and x_{att} is 9 cm (Fig. A1.1a). A change in porosity also implies sediment compaction with depth, and different burial velocities for solutes and solids. The burial velocity of the pore fluid at the end of the integration interval is assumed to be the same as that of the solid phase, i.e. $v_F = v_S$. The depth-dependent advection velocities were calculated from the porosity profile, the constant F_{sed} and the burial velocity at the end of the integration interval using the CRAN:ReacTran package (Soetaert and Meysman, 2012).

The presence of bioturbation is modelled as two different extra transport parameters; bio-mixing and bio-irrigation. Following the conventional description, bio-mixing is modelled as a diffusive process (Boudreau, 1997; Meysman et al., 2010)

$$J_b = -\phi_S D_b \frac{\partial S}{\partial z} \quad [4]$$

Benthic fauna require food resources (organic matter) that arrive from the overlying water at the top of the sediment pile, and thus most of their activity occurs near the sediment-water interface, and decreases with depth (Boudreau, 1998). The bio-diffusivity coefficient accordingly follows a sigmoidal depth profile

$$D_b(z) = D_{b,0} \exp\left(-\frac{(z - x_L)}{0.25 x_{bm}}\right) \Big/ \left(1 + \exp\left(-\frac{(z - x_L)}{0.25 x_{bm}}\right)\right) \quad [5]$$

where $D_{b,0}$ is the bio-diffusivity at the sediment-water interface, x_L is the depth of the mixed layer and x_{bm} is an attenuation coefficient determining the transition zone from mixed to unmixed sediment horizons. For the unbioturbated site, both $D_{b,0}$ and x_L are set to zero, as no burrowing fauna was present. For the bioturbated site, x_L was set to 15 cm, which corresponds to the burrow depth of the two species found at the field site (*Nereis*: 15-20 cm; Esselink and Zwarts, 1989; *Arenicola Marina*: 15-18 cm; Rijken, 1979). The high density of burrows observed in the sediment suggests high bio-mixing activity, therefore, $D_{b,0}$ was set at 10 cm^2 yr^{-1} (Fig. A1.1b).

A second requirement for benthic fauna is oxygen. To keep up the supply of oxygen to the anoxic sediment layers, burrowing animals can actively flush their burrows. This bio-irrigational transport is classically described as a non-local exchange process, where pore-water parcels are exchanged with bottom-water parcels (Boudreau, 1984). Bio-irrigation is implemented using the same relation as bio-mixing,

$$\alpha(z) = \alpha_0 \exp\left(-\frac{\left(z - x_{L,irr}\right)}{0.25 x_{irr}}\right) \Bigg/ \left(1 + \exp\left(-\frac{\left(z - x_{L,irr}\right)}{0.25 x_{irr}}\right)\right) \quad [6]$$

where α_0 is the bio-irrigation coefficient at the sediment-water interface, $x_{L,irr}$ is the depth of the irrigated layer and x_{irr} is an attenuation coefficient determining the transition zone from irrigated to un-irrigated sediment horizons. For the unbioturbated sediment, α_0 and $x_{L,irr}$ were set to zero, while for the bioturbated sediment $x_{L,irr}$ was set to 10 cm and α_0 was calibrated to 1.2 yr^{-1}, based on the NH_4^+ profile, assuming that NH_4^+ acts as tracer (Fig. A1.1c). Following Meile et al. (2005), we introduce solute-specific irrigation coefficients, to capture the differential biogeochemical behaviour of individual pore-water species. For example, the fast oxidation kinetics of Fe^{2+} mean that Fe^{2+} generally is not flushed out of the sediment, but is oxidised in the worm burrow. The solute specific irrigation coefficients were; $\alpha_{Fe^{2+}} = 0$, $\alpha_{SO_4^{2-}} = 5/6 * \alpha$, $\alpha_{HCO_3^-} = \alpha$, $\alpha_{HS^-} = 4/3 * \alpha$, $\alpha_{O_2} = \alpha$, $\alpha_{NH_4^+} = \alpha$, $\alpha_{CH_4} = \alpha$.

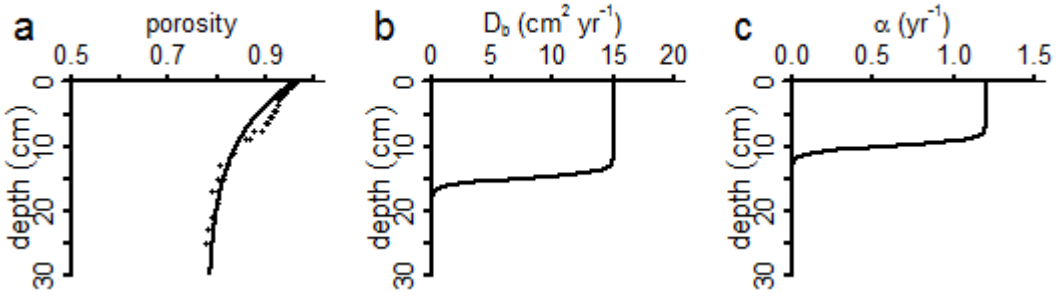

Figure A 1.1: (a) imposed porosity profile, fitted to the porosity profile of the unbioturbated core from October 2015 (black dots). (b) vertical depth profile of the bio-diffusion coefficient and (c) vertical depth profile of the bio-irrigation coefficient in the bioturbated scenario.

Biogeochemical reaction set

The reaction set (n=25, note that there are three different fractions of organic matter, and two fractions of iron oxides) was chosen to be a parsimonious description of the coupled C, Fe

and S cycles in the sediment of the Blakeney salt marsh (Table A 1.1). To keep the numerical simulations tractable, manganese and nitrogen cycling were assumed to be of minor importance, and elemental sulphur was not included. Note that, to match the observed POC depth profile to the sulphate profile, we assumed that organic carbon had an oxidation state of -II. In models, it is conventionally assumed that organic carbon has an oxidation state of 0, but the oxidation state of carbon in organic compounds ranges from -II to +II (Burdige, 2006). Because we have direct observations of the sedimentation velocity and the mass-% of POC, as well as direct measurements of the sulphate concentrations, we believe that these parameters are well constrained. In contrast, we have no data regarding the actual oxidation state of carbon in organic matter. On average, carbon in marine plankton has an oxidation state of -0.3 to -0.7, and marine organic matter that has undergone mineralisation has an oxidation state of -0.6 to -2 (Burdige, 2006). Given the uncertainty of the oxidation state of carbon in organic matter, we believe that the assumption of a low oxidation state for carbon in this case (-2) is acceptable.

Organic matter consists of three fractions; labile organic matter, which is easily degraded and has a high decay constant, slow degradable organic matter, which is degraded at an intermediate rate and refractory organic matter, which is degraded at a slower rate. Each of these fractions can be degraded by four different mineralisation pathways; aerobic respiration (AR), dissimilatory iron reduction (DIR), sulphate reduction (SR) and methanogenesis (MG) (Reactions 1-4; Table A 1.1, note that the same reactions are valid for each of the organic matter fractions). Denitrification and manganese oxide reduction are not included, as they generally contribute little to the total mineralisation rate (Thamdrup, 2000), and the low dissolved Mn concentrations at the field site suggest limited importance of Mn cycling. The classical redox sequence (Froelich et al., 1979) is implemented via conventional limitation-inhibition formulations (Table A 1.2; Soetaert et al., 1996). The reduction of organic matter releases ammonium and bicarbonate in the pore water. Ammonium can adsorb on solid-phase particles (Mackin and Aller, 1984). The adsorption of ammonium is included as a reversible, linear adsorption process, where the concentration of adsorbed ion is in equilibrium at all times with the surrounding pore water, i.e., $\left[X \equiv NH_4^+ \right] = K_{ads}^{NH_4^+} \left[NH_4^+ \right]$, where $K_{ads}^{NH_4^+}$ is the dimensionless adsorption constant (Berg et al., 2003).

Iron oxides are modelled as two separate fractions; fresh iron oxides and aged iron oxides, where the fresh iron oxide fraction can reduce organic matter and oxidise sulphide, and the aged iron oxides only reacts with sulphide (Berg et al., 2003). Organic matter mineralisation coupled to iron oxide reduction released ferrous iron (Fe^{2+}) in the pore water, which can (i) adsorb on

solid-phase particles (Berg et al., 2003), (ii) become re-oxidised by oxygen or (iii) precipitate as iron sulphide (Table A 1.2). Iron oxide reduction coupled to sulphide oxidation immediately captures Fe^{2+} as FeS. Sulphate reduction produces free sulphide, which can be (i) re-oxidised by oxygen, (ii) re-oxidised by iron oxide, (iii) precipitated as FeS, (iv) reaction with FeS to form FeS_2 (Table A 1.2). When all electron acceptors are depleted, methanogenesis produces methane, which can be (i) oxidised by oxygen, or (ii) oxidised by sulphate. The kinetic rate expressions of all re-oxidation processes are described by standard second-order rate laws (Table A1.2). To simplify the reaction set, FeS is assumed to directly precipitate with sulphide-mediated iron reduction (Table A 1.1).

	Kinetic reactions	
R1	Aerobic respiration	$\left\{CH_2.(NH_3)_{1/R_{CN}}\right\}_{f,s,r} + \frac{3}{2}O_2 \rightarrow HCO_3^- + \frac{1}{R_{CN}}NH_4^+ + \frac{R_{CN}-1}{R_{CN}}H^+$
R2	Dissimilatory Iron reduction	$\left\{CH_2.(NH_3)_{1/R_{CN}}\right\}_{f,s,r} + 6FeOOH_f + \frac{11R_{CN}+1}{R_{CN}}H^+ \rightarrow HCO_3^- + \frac{1}{R_{CN}}NH_4^+ + 6Fe^{2+} + 9H_2O$
R3	Sulphate reduction	$\left\{CH_2.(NH_3)_{1/R_{CN}}\right\}_{f,s,r} + \frac{3}{4}SO_4^{2-} + \frac{4-R_{CN}}{4R_{CN}}H^+ \rightarrow HCO_3^- + \frac{1}{R_{CN}}NH_4^+ + \frac{3}{4}HS^-$
R4	Methanogenesis	$\left\{CH_2.(NH_3)_{1/R_{CN}}\right\}_{f,s,r} + \frac{3}{4}H_2O + \frac{4-R_{CN}}{4R_{CN}}H^+ \rightarrow \frac{1}{4}HCO_3^- + \frac{1}{R_{CN}}NH_4^+ + \frac{3}{4}CH_4$
R5a	Ferrous iron oxidation	$4Fe^{2+} + O_2 + 6H_2O \rightarrow 4FeOOH_f + 8H^+$
R5b	Adsorbed iron oxidation	$4X \equiv Fe^{2+} + O_2 + 6H_2O \rightarrow 4FeOOH_f + 8H^+$
R6	Canonical sulphur oxidation	$HS^- + 2O_2 \rightarrow SO_4^{2-} + H^+$
R7	Sulphide-mediated iron reduction	$9HS^- + 8FeOOH_{f,a} + 7H^+ \rightarrow SO_4^{2-} + 8FeS + 12H_2O$
R8	Iron sulphide oxidation	$FeS + \frac{9}{4}O_2 + \frac{3}{2}H_2O \rightarrow FeOOH_f + SO_4^{2-} + 2H^+$
R9	Pyrite precipitation	$FeS + \frac{1}{4}SO_4^{2-} + \frac{3}{4}HS^- + \frac{5}{4}H^+ \rightarrow FeS_2 + H_2O$
R10	Pyrite oxidation	$FeS_2 + \frac{15}{4}O_2 + \frac{5}{2}H_2O \rightarrow 2SO_4^{2-} + FeOOH_f + 4H^+$
R11	Aerobic methane oxidation	$CH_4 + 2O_2 \rightarrow CO_2 + 2H_2O$
R12	Anaerobic methane oxidation	$CH_4 + SO_4^{2-} + H^+ \rightarrow CO_2 + HS^- + 2H_2O$
R13	Iron oxide aging	$FeOOH_f \rightarrow FeOOH_a$
R14	Ferrous iron sorption	$Fe^{2+} \rightarrow X \equiv Fe^{2+}$
R15	Ammonium sorption	$NH_4^+ \rightarrow X \equiv NH_4^+$

Table A 1.1: list of reactions included in the model

Model parametrisation and boundary conditions

Our model analysis aimed to explore the impact of bioturbation on the coupled biogeochemical cycles of C, Fe and S. In the first step, we calibrated our model parameters and boundary conditions on the bioturbated pond of the Blakeney salt marsh (see below), for the parameters where no calibration was required, we used literature values (Table A 1.3). The upper boundary conditions for dissolved constituents was set at fixed concentration, based on *in situ* measurements. The upper boundary conditions for solid-phase species were set at "fixed flux", calibrated on the *in situ* data (see main text). For all species, the lower boundary condition was set at 'no gradient', apart from SO_4^{2-} and HS^-, for which a clear downward gradient was present. For these species, we set the boundary condition at 'fixed concentration'.

Numerical solution

The model includes 14 state variables; the concentrations of labile organic matter $[CH_2O]_f$, slow degradable organic matter $[CH_2O]_s$, refractory organic matter $[CH_2O]_r$, dissolved inorganic carbon $[HCO_3^-]$, dissolved ammonium $[NH_4^+]$ oxygen $[O_2]$, fresh iron oxide $[FeOOH]_f$, aged iron oxide $[FeOOH]_a$, ferrous iron $[Fe^{2+}]$, sulphate $[SO_4^{2-}]$, free sulphide $[H_2S]$, iron sulphide $[FeS]$, pyrite $[FeS_2]$ and methane $[CH_4]$. The open-source programming language R was used to implement a numerical solution procedure for the partial differential equations, following the procedures of Soetaert and Meysman (2012). The spatial derivatives within the partial differential equations (Eq. [1]) were expanded over the sediment grid using finite differences by using the R package CRAN:ReacTran (Soetaert and Meysman, 2012). This sediment grid was generated by dividing the sediment domain (thickness L = 30 cm) into 400 sediment layers of equal thickness. The resulting set of ordinary differential equations was integrated using the stiff equation solver routine 'vode' (Brown et al., 1989) within the package CRAN:deSolve (Soetaert et al., 2010b). All model simulations were run for a sufficiently long time period (>1000 year) to allow them to reach a steady state.

	Kinetic rate expression
	$R_{\min} = \varphi_S k_{\min} [CH_2O]$
R1	$R = R_{\min} \frac{[O_2]}{[O_2] + K_{O_2}}$
R2	$R = R_{\min} \frac{K_{O_2}}{[O_2] + K_{O_2}} \frac{[FeOOH]}{[FeOOH] + K_{FeOOH}}$
R3	$R = R_{\min} \frac{K_{O_2}}{[O_2] + K_{O_2}} \frac{K_{FeOOH}}{[FeOOH] + K_{FeOOH}} \frac{[SO_4^{2-}]}{[SO_4^{2-}] + K_{SO_4^{2-}}}$
R4	$R = R_{\min} \frac{K_{O_2}}{[O_2] + K_{O_2}} \frac{K_{FeOOH}}{[FeOOH] + K_{FeOOH}} \frac{K_{SO_4^{2-}}}{[SO_4^{2-}] + K_{SO_4^{2-}}}$
R5a	$R = \varphi_F k_{FIO} [Fe^{2+}][O_2]$
R5b	$R = \varphi_S k_{FIO} [X \equiv Fe^{2+}][O_2]$
R6	$R = \varphi_F k_{CSO} [HS^-][O_2]$
R7	$R = \varphi_S k_{SMI} [HS^-][FeOOH]$
R8	$R = \varphi_S k_{ISO} [FeS][O_2]$
R9	$R = \varphi_S k_{PyP} [FeS][HS^-]$
R10	$R = \varphi_S k_{PyO} [FeS_2][O_2]$
R11	$R = \varphi_F k_{AMO} [CH_4][O_2]$
R12	$R = \varphi_F k_{AnMO} [CH_4][SO_4^{2-}]$
R13	$R = \varphi_S k_{IOA} [FeOOH_f]$

Table A 1.2: List of kinetic expressions included in the model

ENVIRONMENTAL PARAMETERS	Symbol	Value	Units	Method	References
Temperature	T	10	ºC	A	
Salinity	S	32	-	A	
Porosity (surface value)	ϕ_F^0	0.96	-	A	
Porosity (asymptotic at depth)	ϕ_F^∞	0.78	-	A	
Porosity attenuation coefficient	x_ϕ	9	cm	A	
Solid-phase density	ρ_S	2.0	g cm^{-3}	A	
Sediment accumulation rate	F_{sed}	0.10	g cm^2 yr^{-1}	A	
Depth of sediment domain	L	30	cm	-	
BOUNDARY CONDITIONS	**Symbol**	**Value**	**Units**	**Method**	**References**
Oxygen bottom water	$[O_2]$	0.28	mol m^{-3}	A	
Sulphate bottom water	$[SO_4^{2-}]$	20	mol m^{-3}	A	
DIC bottom water	$\sum CO_2$	3.9	mol m^{-3}	A	
Ammonium bottom water	$[NH_4^+]$	0.01	mol m^{-3}	A	
Ferrous iron bottom water	$[Fe^{2+}]$	0	mol m^{-3}	A	
Free sulphide bottom water	$[HS^-]$	0	mol m^{-3}	A	
Methane bottom water	$[CH_4]$	0	mol m^{-3}	A	
Flux OM fast decaying	F_{OM_F}	17	mmol m^{-2} d^{-1}	B	
Flux OM slow decaying	F_{OM_S}	14	mmol m^{-2} d^{-1}	B	
Flux OM refractory	F_{OM_r}	13	mmol m^{-2} d^{-1}	B	
Flux FeOOH fresh	F_{FeOOH_f}	0.44	mmol m^{-2} d^{-1}	B	
Flux FeOOH aged	F_{FeOOH_a}	0.44	mmol m^{-2} d^{-1}	B	
Flux FeS	F_{FeS}	0	mmol m^{-2} d^{-1}	B	
Flux FeS_2	F_{FeS2}	0	mmol m^{-2} d^{-1}	B	

Table A 1.3: List of parameters included in the model. Solid-phase concentrations are expressed per unit volume of solid phase. "Method" refers to the procedure by which parameter values are constrained: A = Measurements, B = model calibration, C= Literature values. References: [1] Meysman et al., (2003) [2] van de Velde and Meysman (2016), [3] Poulton and Canfield, (2005) [4] Meysman et al., (2015), [5] Berg et al., 2003.

BIOGEOCHEMICAL PARAMETERS	Symbol	Value	Units	Method	References
Mixing depth	L_{mix}	15	cm	B	
Biodiffusion coefficient	D_b	10	$cm^2\ yr^{-1}$	B	
Bio-irrigation coefficient	α_0	1.2	yr^{-1}	B	
Mineralization constant fast	k_f	10	yr^{-1}	B	
Mineralization constant slow	k_s	0.04	yr^{-1}	B	
Mineralization constant refractory	k_r	0.005	yr^{-1}	B	
Oxygen saturation constant	K_{O_2}	0.008	$mol\ m^{-3}$	C	[1]
FeOOH saturation constant	K_{FeOOH}	0.4	$\mu mol\ g^{-1}$	C	[2]
Sulphate saturation constant	$K_{SO_4^{2-}}$	0.9	$mol\ m^{-3}$	C	[1]
C:N ratio organic matter	$C_{org} : N_{org}$	35	-	B	
Ferrous iron oxidation	k_{FIO}	10^{+7}	$\mu mol\ cm^3\ yr^{-1}$	C	[1]
Canonical sulphur oxidation	k_{CSO}	10^{+7}	$\mu mol\ cm^3\ yr^{-1}$	C	[1]
Sulphide-mediated iron reduction	$(k_{SMI})_f$	494	$\mu mol\ cm^3\ yr^{-1}$	C	[3]
Sulphide-mediated iron reduction	$(k_{SMI})_a$	3.6	$\mu mol\ cm^3\ yr^{-1}$	C	[3]
Iron sulphide precipitation	k_{ISP}	10^{+4}	$\mu mol\ cm^3\ yr^{-1}$	C	[4]
Iron sulphide oxidation	k_{ISO}	10^{+7}	$\mu mol\ cm^3\ yr^{-1}$	C	[4]
Pyrite precipitation	k_{PyP}	0.725	$\mu mol\ cm^3\ yr^{-1}$	B	
Pyrite oxidation	k_{PyO}	9.47	$\mu mol\ cm^3\ yr^{-1}$	C	[5]
Aerobic methane oxidation	k_{AMO}	10^{+4}	$\mu mol\ cm^3\ yr^{-1}$	C	[1]
Anaerobic methane oxidation	k_{AnMO}	10	$\mu mol\ cm^3\ yr^{-1}$	C	[1]
Iron oxide ageing	k_{IOA}	0.57	yr^{-1}	C	[5]
Equilibrium constant ferrous iron sorption	$K_{ads}^{Fe^{2+}}$	696	-	C	[5]
Equilibrium constant ammonium sorption	$K_{ads}^{NH_4^+}$	3.84	-	C	[5]

Table A 1.3 continued

Modelled scenarios

In a first step, the model was parameterised to fit the depth profiles in the unbioturbated ponds (Fig. A 1.2). When possible, the model parameters and boundary conditions (concentrations and fluxes) were taken from *in situ* measurements. Other parameters were either calibrated on the depth profiles of the pore-water and solid-phase constituents of the unbioturbated sediment or taken from literature values (Table A 1.3).

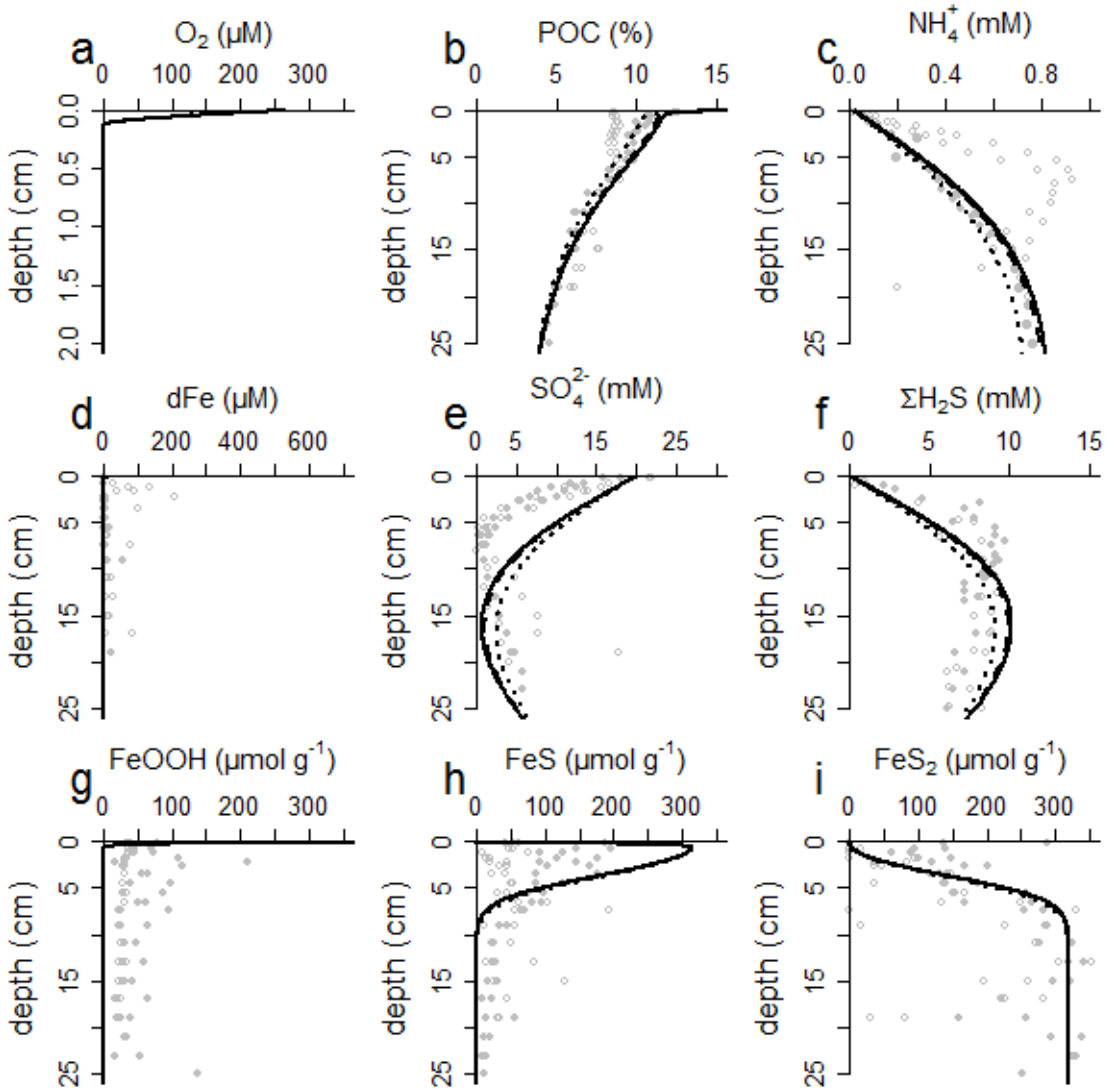

Figure A 1.2: Sensitivity test of the unbioturbated model. Full line = unbioturbated baseline ('U'), Dashed line = aerobic stimulation ('U + AS'), Dotted line = self-priming ('U + SP').

The sediment in the unbioturbated ponds was subsequently modelled using the same parameter set, but extended with extra bioturbation parameters. We explored the effect of bioturbating fauna on the sedimentary cycles of C, Fe and S by running three scenarios; (i) 'Bioturbation' (scenario 'B'), (ii) 'bioturbation + aerobic stimulation' (scenario 'B + AS') and (iii) 'bioturbation + self-priming' (scenario 'B + SP'). In the first scenario ('B'), bioturbation introduces extra transport via bio-mixing ($D_{b,0}$ =10 cm^2 yr^{-1} over 15 cm) and bio-irrigation (α_0 =1.2 yr^{-1} over 10 cm) – see Fig. A 1.1. In the second scenario ('B + AS'), bioturbation introduces extra transport, but we additionally assume that aerobic respiration is more efficient

at breaking down the refractory organic matter fractions (Kristensen, 2000). Non-labile organic matter is broken down 10 times faster by O_2 ($k_{\min,O_2} = 10k_{\min}$). In the third scenario ('B + SP'), bioturbation introduces extra transport, and we assume that the breakdown of the non-labile organic matter fractions is stimulated in the presence of labile organic matter (Canfield, 1994; Burdige, 2007). For this, the kinetic constant of the other organic matter fractions is made dependent on the concentration of fast degradable organic matter ($\left[OC_f\right]$); $k_{\min} = k_{\min,0} + k_{\min,0} f_{priming}(1 - e^{-[OC_f]/[OC_f]_{ref}})$, where $k_{\min,0}$ is the kinetic constant without self-priming, $f_{priming}$ is the priming factor ($f_{priming}$ = 9) and $\left[OC_f\right]_{ref}$ is a reference concentration ($\left[OC_f\right]_{ref}$ = 100 µmol cm^{-3}). The priming factors were derived from model fitting.

The results for all scenarios are shown in Figs A 1.3 – 1.6. None of the tested bioturbation scenarios perfectly match the observed concentration profiles (Figs A 1.3 – 1.6). This could be due to uncertainty in the parameterisation of bioturbation transport, as the high variability in the ^{210}Pb data did not allow us to constrain a mixing intensity or depth (section 3.2 in main text). Additionally, we did not have any direct measurements of the bio-irrigation rate. Furthermore, modelling bio-irrigation in a 1-D diagenetic model remains challenging. For example, whereas the non-local exchange term that we use in our diagenetic model is valid in general (Boudreau, 1984), its parameterisation is solute-dependent, and can differ between situations (Meile et al., 2005). Furthermore, the Fe-S interactions during early diagenesis are very complex, and involve a number of intermediate reaction steps (Jørgensen et al., 2019) that are not represented in our model because of numerical efficiency and lack of proper rate constraints.

Nevertheless, the model simulation with priming ("scenario B + SP") and high bio-irrigation (1.2 yr^{-1}) does capture the important trends in the depth profiles (dash-dotted line in Fig. A 1.6), and so we believe the modelled reaction rates provide a representative picture of the natural situation. As it happens, the simulated sulphate reduction rate (14.7 mmol S m^{-2} d^{-1}) agrees with the depth-integrated sulphate reduction rate of 14.2 mmol S m^{-2} d^{-1} previously measured in slurry incubation experiments using bioturbated salt marsh sediments from Blakeney (Mills et al., 2016).

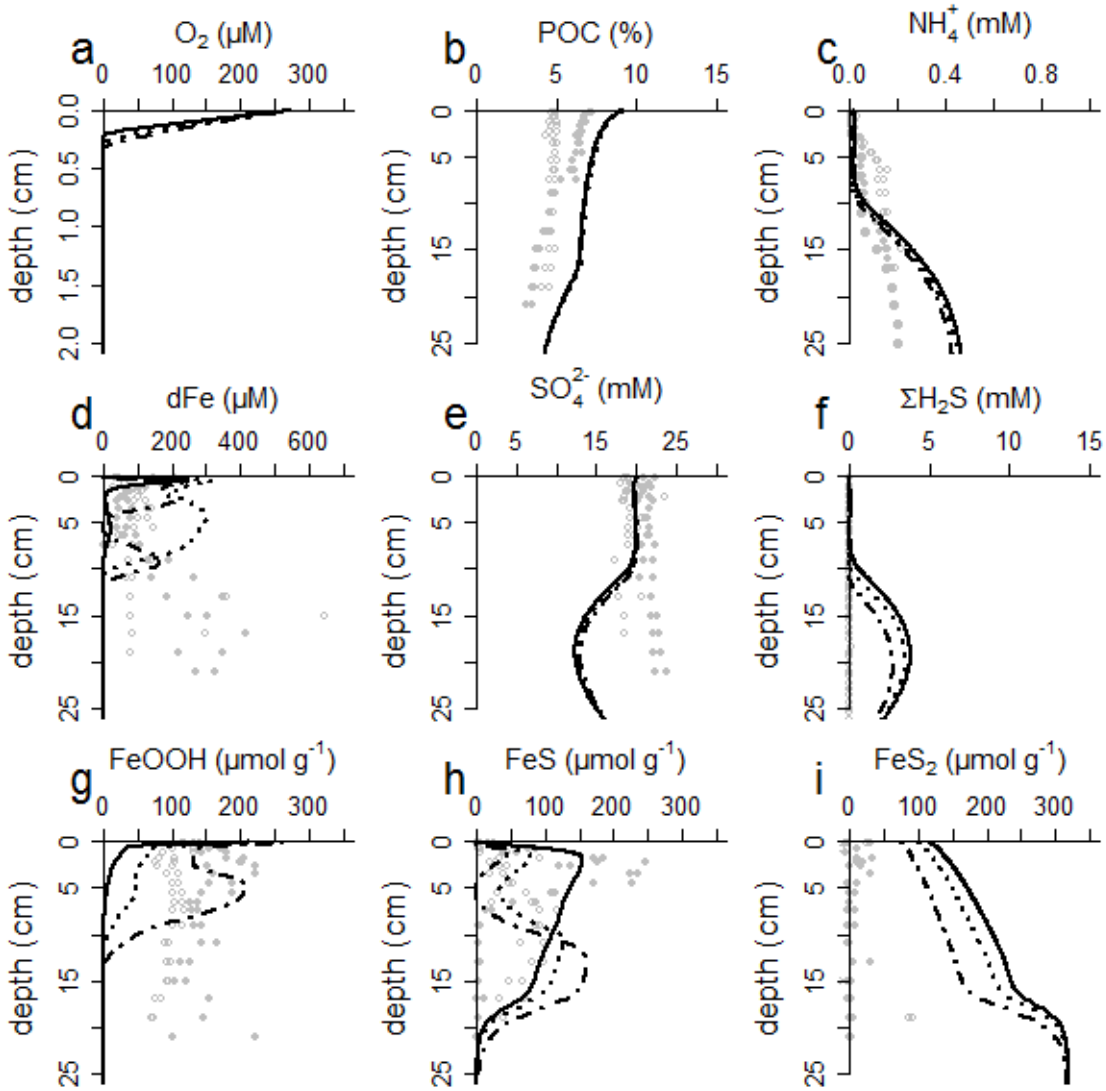

1156

1157 **Figure A 1.3:** Sensitivity test of the bioturbated baseline model (scenario 'B') with higher bio-irrigation. Full line $\alpha_0 = 0.5$ yr^{-1}, Dashed line $\alpha_0 = 0.75$ yr^{-1}, Dotted line $\alpha_0 = 1$ yr^{-1}, Dash-dotted line $\alpha_0 = 1.2$ yr^{-1}

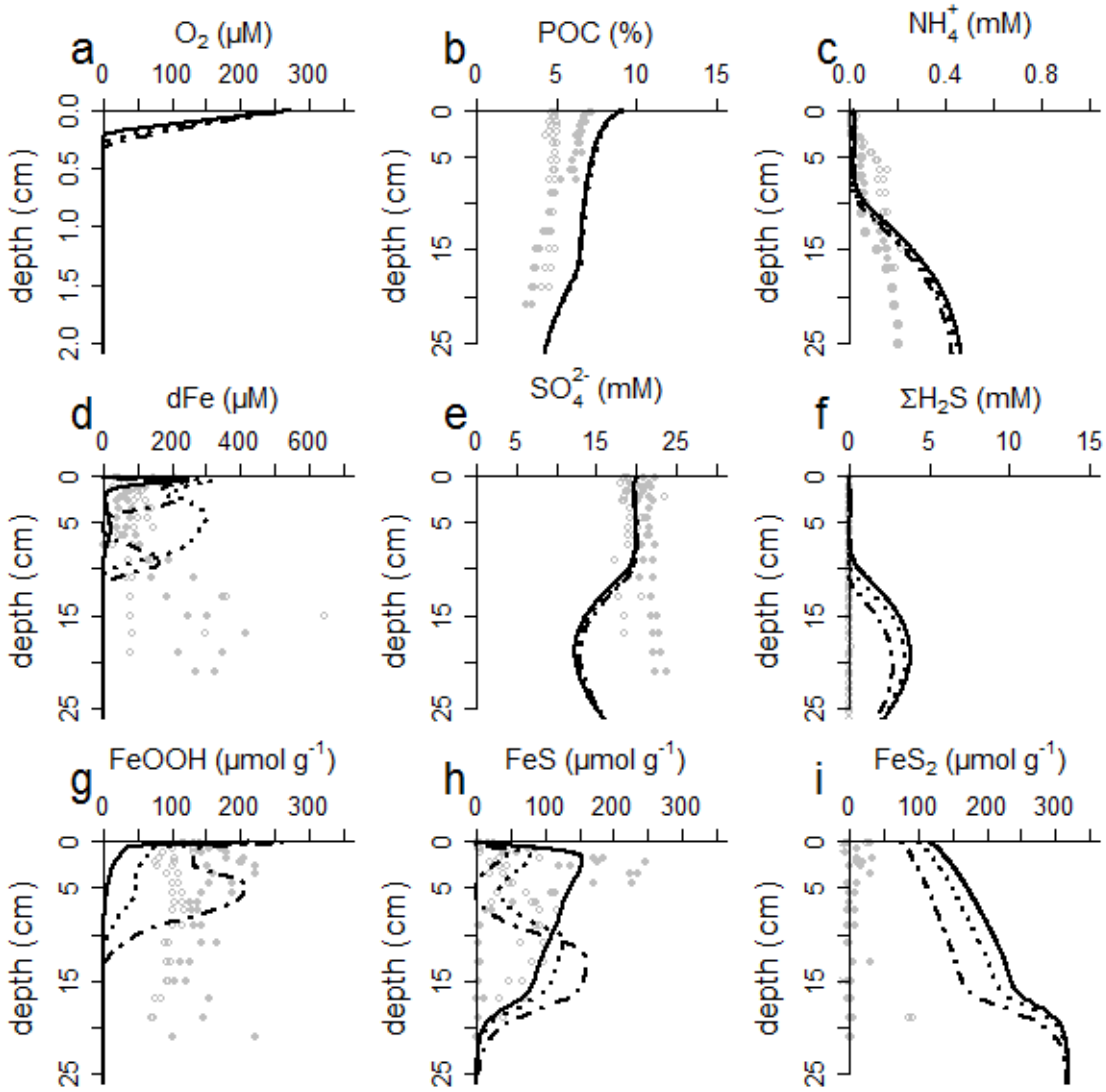

Figure A 1.4: Sensitivity test of the bioturbated aerobic stimulation model (scenario 'B + AS') with higher bio-irrigation. Full line $\alpha_0 = 0.5$ yr^{-1}, Dashed line $\alpha_0 = 0.75$ yr^{-1}, Dotted line $\alpha_0 = 1$ yr^{-1}, Dash-dotted line $\alpha_0 = 1.2$ yr^{-1}

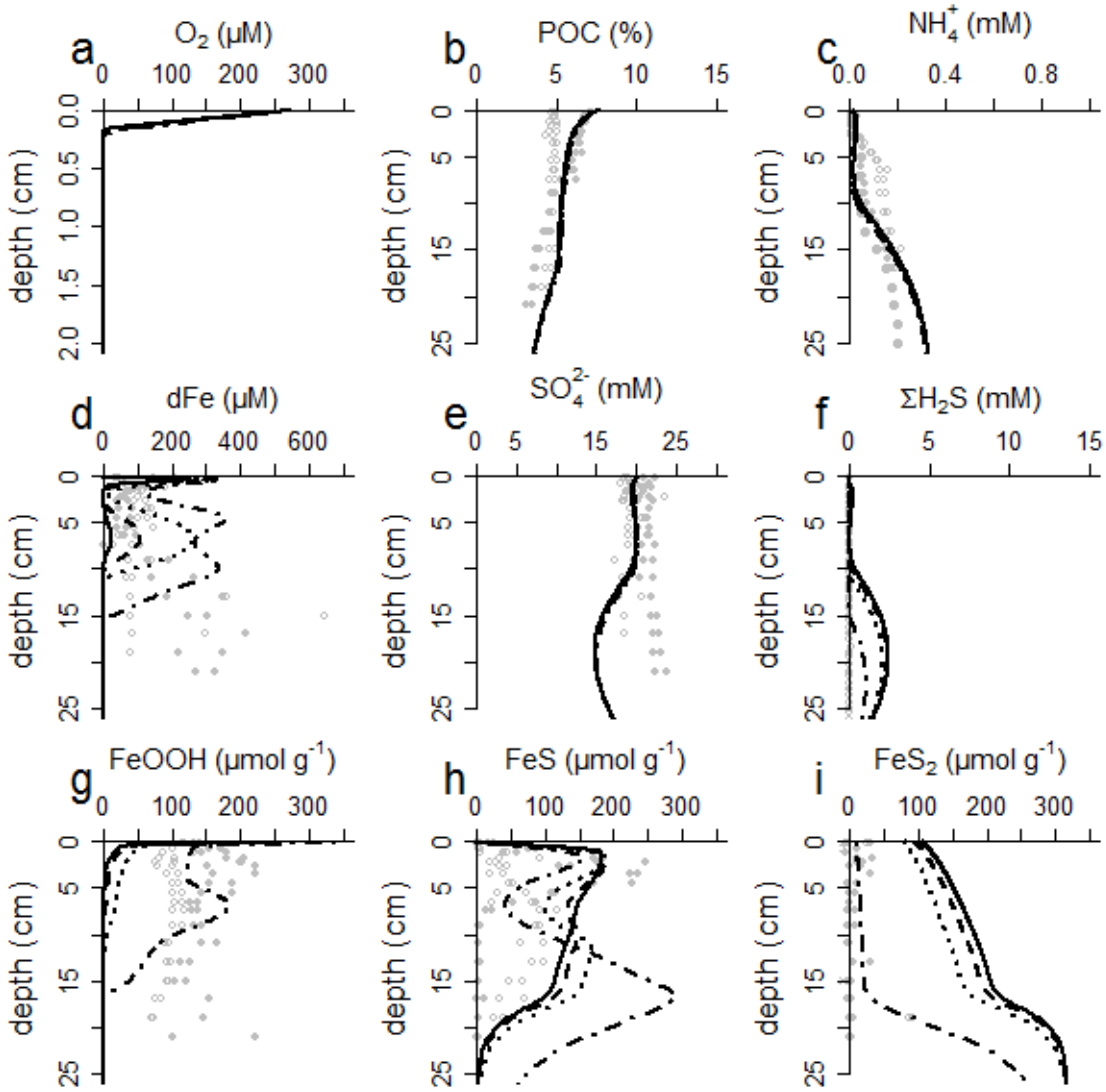

Figure A 1.5: Sensitivity test of the bioturbated self-priming model (scenario 'B + SP') with higher bio-irrigation. Full line $\alpha_0 = 0.5\ yr^{-1}$, Dashed line $\alpha_0 = 0.75\ yr^{-1}$, Dotted line $\alpha_0 = 1\ yr^{-1}$, Dash-dotted line $\alpha_0 = 1.2\ yr^{-1}$

Appendix 2: Organic matter balance

Estimation of organic matter mineralisation rate

To examine the organic carbon balance in the sediment, we can write a simplified mass balance for POC as

$$L\frac{dC}{dt} = \left(J_{input} - J_{burial}\right) - R_{\min} \quad [7]$$

In this, L is thickness of the sediment domain that is considered, J_{input} is the input of organic carbon at the sediment-water interface, J_{burial} is the burial flux of organic carbon and $R_{\min}$ is the depth-integrated mineralization rate of organic carbon. At steady state, the POC balance is given by

$$R_{\min} = J_{input} - J_{burial} \quad [8]$$

We further detail this POC budget for the unbioturbated sediment using the POC depth profile and diffusive fluxes of solutes, as estimated in the previous section. For the bioturbated sediment, this cannot be done, as the presence of bio-irrigation and bio-mixing implies that solute fluxes are not exclusively governed by molecular diffusion and that solid-phase transport is not only driven by sedimentation.

We can estimate the mineralisation rate $R_{\min}$ in the unbioturbated pond in 4 alternative ways (based on particulate organic carbon, ammonium, sulphide or sulphate depth profiles). Foremost, in an unbioturbated sediment, where solid-phase transport is only governed by downward advection of accumulating sediment, the flux at any given depth horizon is given by $J_X = J_s C_X$, where C_X is the concentration of a given solid phase component (this relation assumes steady-state compaction; Meysman et al., 2005). If we apply this to POC, the input of organic carbon at the sediment-water interface for the unbioturbated pond is 26 ± 9 mmol C m^{-2} d^{-1} in October 2015 and 18 ± 6 mmol C m^{-2} d^{-1} in August 2016 (Table 2 in main text). Similarly, the burial flux of POC becomes 10 ± 3 mmol C m^{-2} d^{-1} in October 2015 and 12 ± 4 mmol C m^{-2} d^{-1} in August 2016 (see main text). The mineralisation rate R_{min} can then be estimated as the difference between both quantities, as 16 ± 9 mmol C m^{-2} d^{-1} in October 2015 and 6 ± 7 mmol C m^{-2} d^{-1} in August 2016. The variation between ponds is likely caused by local differences in organic matter delivery, or spatial heterogeneity within the ponds.

Alternatively, the mineralisation rate can be estimated from the ammonium production in the sediment. If we assume that all organic nitrogen is released by mineralisation as NH_4^+, and there is no significant oxidation of ammonium (e.g. through nitrification or anammox), the

mineralisation rate can be estimated as

$$R_{\min} = -\left(\frac{C_{org}}{N_{org}}\right)\left(J_{diff,SWI}^{NH_4^+} - J_{diff,deep}^{NH_4^+}\right) \quad [9]$$

This leads to an R_{min} in the unbioturbated pond of 5.8 ± 0.5 mmol C m^{-2} d^{-2} for October 2015 and 25 ± 4 mmol C m^{-2} d^{-2} for August.

Thirdly, in unbioturbated sediments with a shallow oxygen penetration depth, most organic matter is mineralised via sulphate reduction. Accordingly, we can approximate R_{min} as

$$R_{\min} = -\tfrac{4}{3}\left(J_{H_2S,diff,SWI} - J_{H_2S,diff,deep} - J_{S,burial}\right) \quad [10]$$

In this, $J_{S,burial}$ represents the burial of solid-phase sulphur (iron sulphides and elemental sulphur) at depth and 4/3 represents the stoichiometric coefficient for sulphate reduction (4 moles of carbon oxidised per 3 moles of sulphate reduced, which is valid if carbon in organic matter has an oxidation state of -II; see Appendix 1). This leads to an R_{min} of 28.7 ± 0.3 mmol C m^{-2} d^{-1} in October 2015 and 24.7 ± 0.3 mmol C m^{-2} d^{-1} in August 2016. In a similar way, R_{min} can be calculated using the sulphate uptake of the sediment

$$R_{\min} = \tfrac{4}{3}\left(J_{SO_4^{2-},diff,SWI} - J_{SO_4^{2-},diff,deep}\right) \quad [11]$$

which equals 21.3 mmol C m^{-2} d^{-1} in October 2015 and 33.5 mmol C m^{-2} d^{-1} in August, remarkably close to the estimate based on the sulphide balance, which suggests that the sulphur cycle is close to steady state.

It is quite likely that the POC profile underestimates the true mineralisation rate, due to the coarse core slicing. We actually integrate the upper 0.5 cm of the sediment core, and thus likely underestimate the true POC flux at the SWI. Additionally, the solid phase is prone to spatial heterogeneity, as solid-phase particles cannot diffuse like dissolved species. Therefore, we focus on the mass balance made using the dissolved species. The nitrogen approach estimates a mineralisation rate that is about half of the sulphur approach. This can be because the bulk C:N ratio we use does not adequately represent that of the organic matter being mineralised, or because there is an ammonium sink we have not identified. Inversely, we could be overestimating the mineralisation rate estimated via the sulphur balance because we do not know the actual oxidation state of the carbon in organic matter, although that is quite unlikely, since we already assumed -II, which is the lowest value reported for marine sediments so far (Burdige, 2006). Given the uncertainty that is associated with both the nitrogen and sulphur approach, we will use the estimates as a range ($5.8 < R_{min} < 33.5$ mmol C m^{-2} d^{-1}) for the rest of the discussion.

With the R_{min} estimated, we can calculate the actual organic matter influx in the unbioturbated pond as $12.8 < J_{POC,in} < 46.5$ mmol C m^{-2} d^{-1} for October 2015 and $13.8 < J_{POC,in} < 49.5$ mmol C m^{-2} d^{-1} for August 2016.

Organic carbon mass budget

We can rewrite equation [7] as

$$L\frac{d\hat{C}}{dt} = \left(J_{input} - \nu_{sed}\hat{C}\right) - k\hat{C}L \qquad [12]$$

where concentration $\hat{C} = (1-\phi_{AVG})\rho_s C$ is the bulk volumetric POC where ϕ_{AVG} is the average porosity and ρ_s is the solid-phase density in the sediment domain. At steady state ($d\hat{C}/dt = 0$), one obtains a simple relation for the key factors that control the magnitude of the mean POC

$$\hat{C} = \frac{J_{input}}{\left(kL + \nu_{sed}\right)} \qquad [13]$$

where the sedimentation velocity ν_{sed} is 0.3 cm yr^{-1}, and similar in both the bioturbated and unbioturbated ponds (see main text). Hence, the factors that explain the difference in the mean POC concentration are either that the organic input J_{input} is lower in the bioturbated ponds, or that the intrinsic mineralisation rate k is higher in the bioturbated ponds.

The mean POC concentration is ~37% higher in the unbioturbated ponds (5.1 ± 0.9 % in the bioturbated ponds versus 7 ± 2 % in the unbioturbated pond). If J_{input} is the only factor affecting the mean POC concentration, then the POC input also has to be 37% lower in the bioturbated ponds, since

$$\frac{\hat{C}_{unb}}{\hat{C}_{biot}} = \frac{J_{input,unb}}{\left(kL + \nu_{sed}\right)} \Big/ \frac{J_{input,biot}}{\left(kL + \nu_{sed}\right)} = \frac{J_{input,unb}}{J_{input,biot}} \qquad [14]$$

and thus

$$\frac{\hat{C}_{unb}}{\hat{C}_{biot}} = 1.37 = \frac{J_{input,unb}}{J_{input,biot}} \qquad [15]$$

or

$$J_{input,unb} = 1.37 J_{input,biot} \qquad [16]$$

Inversely, if the intrinsic mineralisation rate k is the only factor affecting

$$\frac{\hat{C}_{unb}}{\hat{C}_{biot}} = \frac{J_{input}}{\left(k_{unb}L + \nu_{sed}\right)} \Big/ \frac{J_{input}}{\left(k_{biot}L + \nu_{sed}\right)} = \frac{k_{biot}L + \nu_{sed}}{k_{unb}L + \nu_{sed}} \qquad [17]$$

and

$$\frac{\hat{C}_{unb}}{\hat{C}_{biot}} = 1.37 = \frac{k_{biot}L + \nu_{sed}}{k_{unb}L + \nu_{sed}} \quad [18]$$

then

$$k_{biot}L + \nu_{sed} = 1.37k_{unb}L + 1.37\nu_{sed} \quad [19]$$

and

$$k_{biot} = 1.37k_{unb} + 0.37\frac{\nu_{sed}}{L} \quad [20]$$

We can estimate the difference in mineralisation rate by using our estimate for the carbon J_{input} , derived above (13-50 mmol m^{-2} d^{-1}), and the calculated burial rate in both pond types (see main text). The POC burial rate in the unbioturbated pond is 7-16 mmol m^{-2} d^{-1}, and 5-12 mmol m^{-2} d^{-1} in the bioturbated ponds. Assuming that J_{input} is the same, the total mineralisation in the unbioturbated pond is 6-34 mmol m^{-2} d^{-1}, and 8-38 mmol m^{-2} d^{-1} in the bioturbated pond. This means that the mineralisation in the bioturbated pond is increased by 12 – 33 %.

Appendix 3: Extra tables

Fraction	Extraction solution	Extraction time	Ref.
Fe_{carb}	1 M sodium acetate, buffered to pH 4.5 with acetic acid Solvent: milli-Q	24h	(Poulton and Canfield, 2005)
Fe_{ox1}	1 M hydroxylamine hydrochloride Solvent: 25 % v/v acetic acid – milli-Q	24h	(Poulton and Canfield, 2005)
Fe_{ox2}	50 g L^{-1} sodium dithionite Solvent: 25 % v/v acetic acid – milli-Q	2h	(Poulton and Canfield, 2005)
Fe_{mag}	0.2 M ammonium oxalate + 0.17 M oxalic acid Solvent: milli-Q	2h	(Poulton and Canfield, 2005)
Fe_{AVS} AVS	6 M HCl Solvent: milli-Q	40 min.	(Kallmeyer et al., 2004) (Canfield et al., 1986) (Cornwell and Morse, 1987)
Fe_{CRS} CRS	N,N di-methyl formamide Chromium solution: 125 g CrCl3.6H2O + 21 mL 37% HCl, bubbled for 20 min. with activated Zinc granules Solvent: milli-Q	40 min.	(Kallmeyer et al., 2004) (Canfield et al., 1986) (Cornwell and Morse, 1987)
S^0	Methanol	Overnight	(Kamyshny et al., 2009)

Table A 1: Summary of all employed extraction solutions and times in the solid-phase speciation of iron and sulphur. See main text for details

Parameter	Symbol	Unit	Value	
			Unbioturbated	*Bioturbated*
sediment accumulation rate (SAR)	v	cm yr^{-1}	0.3 ± 0.1	n.d.
average solid-phase density	$\rho_{solid,av}$	g cm^{-3}	2.2 ± 0.2	2.1 ± 0.2
average porosity	ϕ_{AVG}	-	0.88 ± 0.06	0.79 ± 0.09
sediment flux based on ^{210}Pb profile	J_s	**kg m^{-2} yr^{-1}**	**0.8 ± 0.2**	**n.d.**
Depth of ^{137}Cs peak	L	cm	15	11
Porosity at sediment-water interface	$\phi_{x=0cm}$	-	0.96	0.92
Porosity at depth L	$\phi_{x=L}$	-	0.81	0.73
sediment flux based on ^{137}Cs profile	J_s	**kg m^{-2} yr^{-1}**	**0.91 ± 0.08**	**0.86 ± 0.08**

Table A 2: Parameters used in the calculations of the sediment flux.

Appendix 4: Extra Figures

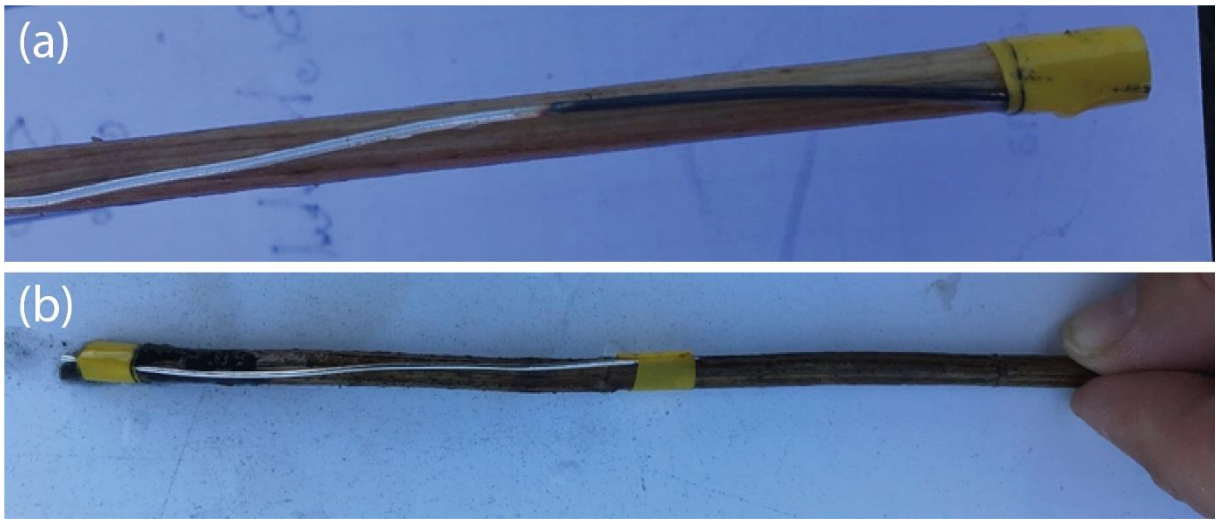

Figure A 1: (a) Picture of silver wire from a non-bioturbated pond. (b) Picture of silver wire from a bioturbated pond. The black colour is evidence for the presence of pore-water sulphide.

Figure A 2: Picture of the rhizon extraction set-up.

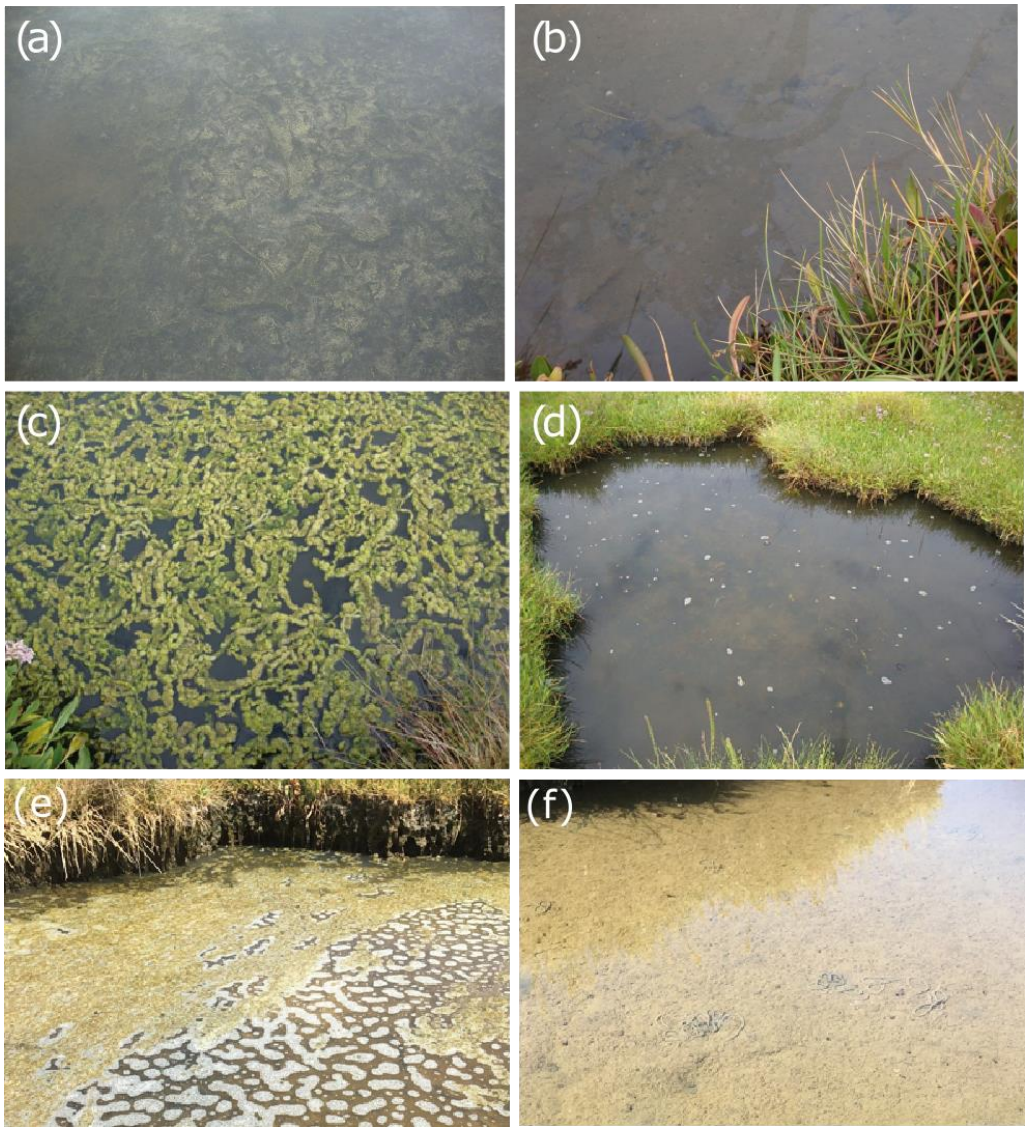

Figure A 3: (a) Picture of an unbioturbated pond in October 2015. (b) Picture of a bioturbated pond in October 2015. (c) Picture of an unbioturbated pond in August 2016. (d) Picture of a bioturbated pond in August 2016. (e) Picture of an unbioturbated pond in August 2018. (f) Picture of a bioturbated pond in August 2018.

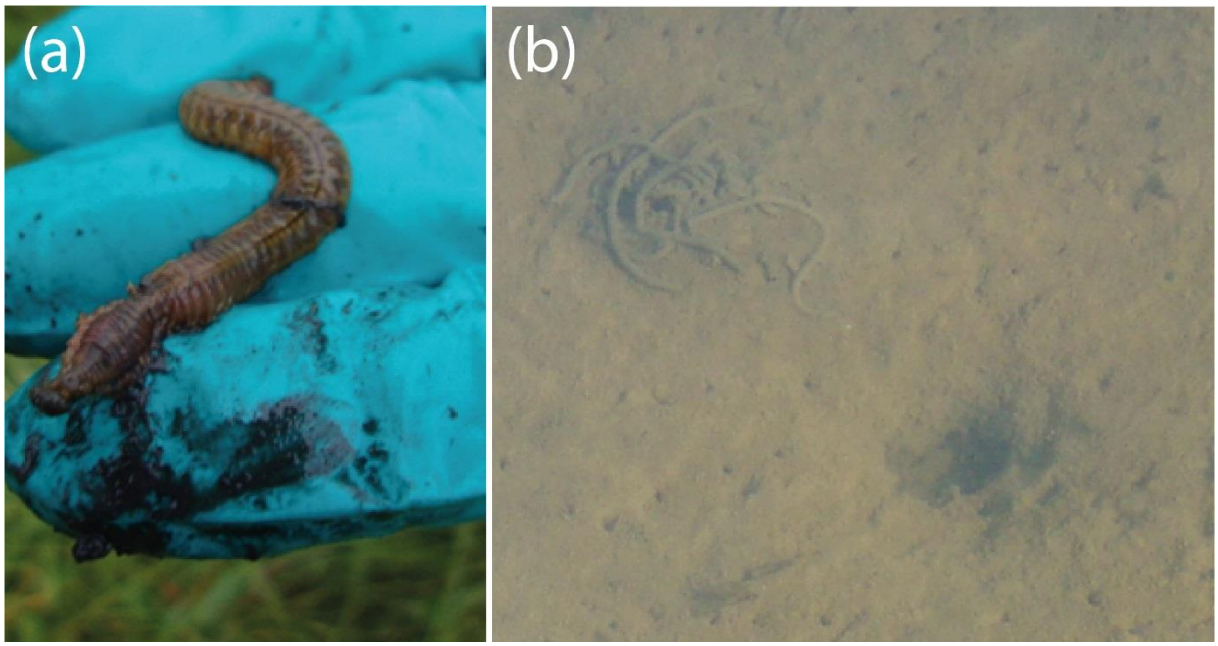

Figure A 4: (a) Picture of *Nereis* spp. found at the field site. (b) Visual evidence of the presence of *Arenicola* spp.

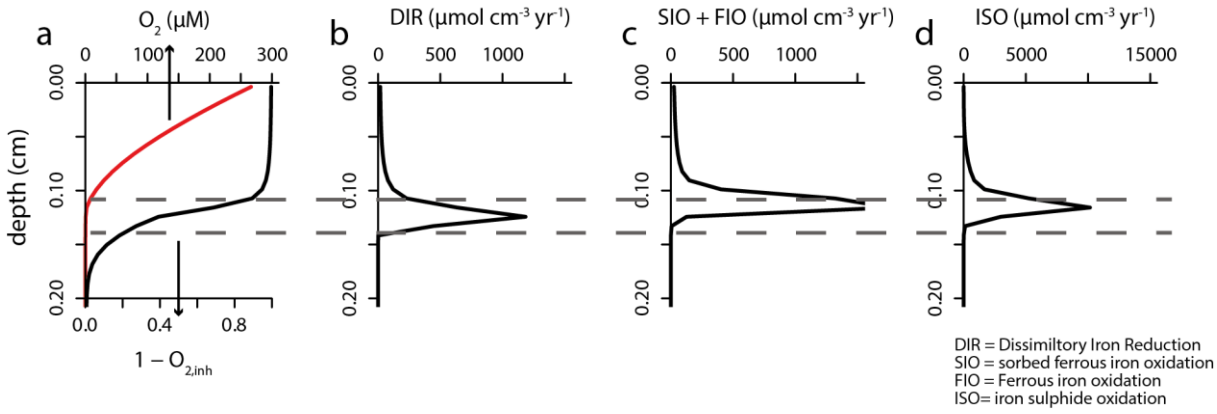

Figure A 5: Reaction rates associated with the cryptic iron cycle (see main text).